LBL-9941

Lawrence Berkeley Laboratory
UNIVERSITY OF CALIFORNIA

Materials & Molecular
Research Division

THE EFFECTS OF COMPOSITION AND HEAT TREATMENTS ON THE STRENGTH AND DUCTILITY OF Fe-Cr-Co ALLOYS

Kenneth G. Kubarych
(Ph.D. thesis)

June 1980

Prepared for the U.S. Department of Energy under Contract W-7405-ENG-48

LBL-9941

THE EFFECTS OF COMPOSITION AND HEAT TREATMENTS ON THE STRENGTH AND DUCTILITY OF Fe-Cr-Co ALLOYS

by

Kenneth C. Kubarych
(Ph.D. thesis)

June 1980

Materials Science and Mineral Engineering Department
Materials and Molecular Research Division
Lawrence Berkeley Laboratory
University of California
Berkeley, California 94720

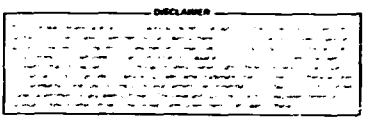

TABLE OF CONTENTS

ABSTRACT

The relationship between the microstructure and mechanical properties of spinodally decomposed Fe-Cr-Co ductile permanent magnet alloys has been investigated using transmission electron microscopy, electron diffraction, tensile testing, and Charpy impact testing. Isothermal aging and step aging of four alloys (Fe-28wt%Cr-15wt%Co, Fe-23wt%Cr-15-wt%Co-5wt%V, Fe-23wt%Cr-15wt%Co-3wt%V-2wt%Ti, and Fe-31wt%Cr-23% Co) resulted in decomposition into two phases, an Fe-Co rich (α_1) phase and a Cr rich (α_2) phase. The microstructural features of the decomposition products were consistent with those expected from a spinodal reaction and agree with the reported work on the Fe-Cr-Co system. An Fe-23wt%Cr-15wt%Co-5wt%V alloy was found to have, among the four alloys, the best combinations of strength and ductility.

Isothermal aging of the alloys increased their strength appreciably, however, this increase in strength is accompanied by severe embrittlement. Two forms of embrittlement were detected. At higher aging temperatures (e.g. 640^{o}C) a grain boundary σ phase was formed, primarily resulting in lowered Charpy impact toughness values. At lower aging temperatures (e.g. 600^{o}C) matrix embrittlement occurred, which greatly reduced the tensile ductility and the Charpy impact toughness. This embrittlement has been attributed to the enrichment in Chromium of the α_2 phase, resulting in it being embrittled. The alloying additions of V and V + Ti retard the embrittlement by allowing a reduction in the grain size, but they do not eliminate the embrittlement. The application of a thermomechanical treatment, in addition, was found to improve ductility.

Fundamentals of the hardening due to spinodal decomposition are

discussed as is their relationship to previous work on the Fe-Cr system. The hardening is attributed to a combination of three mechanisms. These are based on the elastic interactions between dislocations and precipitates the difference in elastic modulii between precipitate and matrix, and the energy required in breaking chemical bonds when a dislocation cuts through the precipitate.

I. INTRODUCTION

Development of permanent magnet alloys that not only possess good magnetic properties but also exhibit sufficient ductility to facilitate their processing into complicated shapes is an area of great metallurgical interest. The recent work of Kaneko et al. (1) has demonstrated that the alloys based on the Fe-Cr-Co ternary system not only have excellent magnetic properties but are ductile prior to magnetic aging. These Fe-Cr-Co alloys have been suggested as possible replacements for the presently used ductile permanent magnet materials (e.g. Fe-Co-V, Cu-Ni-Fe, Fe-Co-Mo alloys) and some of the Alnico alloys (e.g. Alnico V). Figure 1 shows the demagnetizing fields of several ductile magnets and an Fe-Cr-Co alloy. Clearly, the Fe-Cr-Co alloy has magnetic properties superior to the other available materials. The magnetic properties of the Fe-Cr-Co alloys can equal those of some of the Alnico alloys; yet, are far easier to manufacture into finished pieces. Whereas parts made from Alnico alloys must be either cast or sintered, fabrication of magnetic parts with the Fe-Cr-Co alloys may be done using standard metal working techniques (e.g. rolling, stamping, etc.).

Recently the Fe-Cr-Co alloys have been introduced as possible commercial replacements to the ductile Remalloy (Fe-Co-Mo) presently in use in the telephone industry. Telephone receivers require a cup-shaped permanent magnet that is traditionally made from Remalloy, which must be stamped at 1250°C. An alloy based on the Fe-Cr-Co system, called Chromindur,(2), has been developed to take advantage of the alloy's ductility so that the pieces may be stamped at room temperature while maintaining magnetic properties comparable to those of the Remalloy.

The four main parameters that describe magnetic properties are: saturation magnetization ($4\pi I_s$), remanent magnetization (Br), coercive force (Hc), and the energy product ((BH) max). Only the saturation magnetization is not a structure sensitive property, whereas the other three properties may be affected by metallurgical processing. This allows the possibility of technologically controlling the magnetic properties by controlling the microstructural features.

In general, there are two types of magnetic hardening mechanisms (3). In one case, the matrix material is ferromagnetic and the motion of domain boundaries is impeded by dislocations, inclusions, and precipitates (e.g. magnet steels, Fe-Co-Mo (Remalloy), some rare earth magnets). In the other case, small ferromagnetic particles below a critical size at which domain walls cease to exist are embedded in a nonmagnetic matrix. In this case, the magnetic particles are single domains and to change the direction of the magnetization requires a rotation of the magnetic moments of the single domain particles since there are no domain boundaries present. The single domain particle mechanism is usually considered to give higher coercive forces. The required morphology for single domain particle magnets has been produced by powder metallurgy (e.g. Ba-Ferrite and some rare-earth Cobalt magnets) and by spinodal decomposition (e.g. Cu-Ni-Fe, Alnico, and Pt-Co alloys, and some rare-earth Cobalt magnets containing Cu).

The Fe-Cr-Co alloys are age hardenable magnetic alloys that also derive their excellent magnetic properties from spinodal decomposition. When the material is aged inside the miscibility gap, decomposition into two isomorphous phases occurs, one Fe-Co rich (α_1) and the other Cr-rich (α_2). It is reported that the magnetization reversal process

of an Fe-23Cr-15Co-5V alloy occurs by domain wall pinning as opposed to single domain particles (4). The domain walls in the Cr-rich (α_2) phase get pinned by the Fe-Co rich (α_1) particles which implies that the Curie temperature of the α_2 phase is above room temperature. However, if the composition of the α_2 phase is altered so that the phase is paramagnetic, the magnetization mechanism will become a single domain particle mechanism.

In addition to the effects on the magnetic properties of alloys, spinodal decomposition also has profound effects on the mechanical hardening of alloys. Considerable effort has been directed toward studying the mechanical properties of spinodally decomposed alloys (5-11). Generally, the increase in yield strength of the aged material is most sensitive to the difference in lattice parameter between the two decomposing phases (7, 8, 9, 11). The lattice parameter difference is solely a function of the aging temperature since, as lower aging temperatures are used, greater phase separation occurs, which in turn increases the difference in the composition and the lattice parameter between the two phases.

The presence of the miscibility gap in the Fe-Cr-Co ternary system is an extension of the miscibility gap from the binary Fe-Cr system. Many Fe-Cr alloys show a remarkable age hardening response; unfortunately, associated with this increase in strength the material is severely embrittled. The embrittlement of the aged material is believed to be a direct consequence of the decomposition products (12). This has come to be known as "475°C embrittlement" and differs from the embrittlement of stainless steels containing Cr (13). The embrittlement of stainless steels held for long times at elevated temperatures

is due to the formation of a grain boundary σ phase. Sigma is a hard brittle Chromium rich phase, whose sluggish growth kinetics favor formation at grain boundaries. The presence of σ in the aged Fe-Cr-Co alloys has been detected (14). The phase is nonmagnetic. Due to its relatively small volume fraction, it has only minor effects on the magnetic properties of the alloys. The mechanical properties, however, as as with the stainless steels, may be significantly affected by the presence of sigma.

Controlling physical properties of a material by altering its microstructure is a fundamental procedure in materials science. Spinodal decomposition is a phase transformation that allows such control, and the microstructural effect on the magnetic properties of the Fe-Cr-Co alloys has been very thoroughly studied (4, 14-18). Yet to date, little information on the mechanical properties of the Fe-Cr-Co alloys and their relationship to the microstructural features exist in the literature. It is the intent of this work to investigate the effects of alloy compositions and heat treatments on the mechanical properties of the Fe-Cr-Co alloys. Here, the mechanical properties have been measured by tensile testing and Charpy impact testing. The morphology and the microstructural details have been investigated by transmission electron microscopy, scanning electron microscopy, and optical metallography. Finally, the correlation between the microstructure and the mechanical properties has been established.

II. LITERATURE REVIEW

Investigations of the Fe-Cr-Co ternary phase diagram have been made by Köster (19), Rideout et al. (20), and Köster and Hofman (21). Figure 2a-c are the isothermal sections at 1200°C, 700°C, and 600°C, respectively. Figure 2a shows two solid solution fields (one γ (fcc) phase and one α (bcc) phase) along with their relationship to the phase that extends from the Co-Cr binary system. At lower temperatures, the σ phase field stretches across the ternary diagram from the Co-Cr binary to the Fe-Cr binary (Fig. 2b,c). However, no sections of the diagram below 600°C were mentioned in this work.

The existence of a miscibility gap in the Fe-Cr binary system was first suggested through the work of Fisher, Dulis, and Carroll (22). They found spherical precipitates about 200Å in diameter in a 28.5 at .% steel aged 1 to 3 years at 475°C. The precipitates were nonmagnetic, had a bcc structure with a lattice parameter between those of pure Fe and Cr and contained approximately 80 at .% Cr. Neutron diffraction studies (23) indicated clustering when aged at 475°C. Williams and Paxton (24) and Williams (25) confirmed these results and proposed the existence of a miscibility gap below the σ phase region in the phase diagram. Similar results were obtained by Marcinkowski, Fisher, and Szirmae (26).

Spinodal decomposition as the mode of decomposition in the Fe-Cr binary system was first proposed by Imai, Izumiyana, and Matsuno (27) on the basis of magnetic and electrochemical measurements. Lagneborg (28) studying an Fe-30Cr alloy aged at either 475°C or 550°C concluded that the phase separation occurred by spinodal decomposition at the lower temperature but by nucleation and growth at the higher temperature. The electron microscopic results of Vintaikin et al. (29) also suggest the possibility of spinodal decomposition. These suggestions of spinodal

decomposition are based on indirect evidence; however, work using Mössbauer spectroscopy has directly identified the phase separation to be by spinodal decomposition. Chandra and Schwartz (30) confirmed the existence of a miscibility gap and that phase separation proceeded by spinodal decomposition in an Fe-60Cr alloy. They also determined that decomposition by nucleation and growth occurred with compositions of 12-30 at .% Cr when aged at 475°C.

Kaneko, Homma, and Minowa (1) discovered that additions of Cobalt to the Fe-Cr binary extended the miscibility gap into the ternary system. It was determined that spinodal decomposition was the mode of phase separation which had been confirmed by Mössbauer spectroscopy (31). The initial alloys studied required high solution treating temperatures in order to obtain a single α phase and a very rapid quench to avoid the formation of a γ or σ phase. This led to the further alloying with the so called α stabilizing elements (eg. Si, Mo, V, Al, Nb, Ti, etc.) (2,15,32-35). The additions of these elements reduced the size of the γ-loop resulting in easier heat treating requirements. Figure 3 shows the phases present after 1 hour holding time for a section through the ternary diagram with the Co content held at 15%. The reasons for the high solution treating temperature and rapid quench are clearly shown. The effects of the additions of the stabilizing elements are demonstrated in Figs. 4 and 5. In this case, the Co content is held constant at 15 wt% but 5 wt% Cr is replaced with either V or V + Ti. The additions of either the V or V + Ti produced quite a remarkable change in the diagrams. The solution treating temperature may be lowered and the quenching requirements are eased; in fact, the technique of continuous cooling has been successfully applied (4).

The approximate shape of the miscibility gap in the Fe-Cr-Co ternary system has been determined by Kaneko et al (36) using mechanical hardness and Curie temperature measurements. Figure 6a shows the miscibility gap in the α phase of the Fe-Cr-Co system. Also shown are the approximate decomposition lines denoted by A, B, C, and D and the pseudo-binary diagrams associated with these lines are shown in Fig. 6b. The Fe-Cr pseudo-binary is shown for comparison. The shape of the miscibility gap changes quite noticeably with increasing amounts of Co. The peak of the miscibility gap is shifted toward the Fe-rich side of the diagram and to higher temperatures. This tends to skew the miscibility gap so that it is asymmetric. The asymmetric shape of the miscibility gap makes the composition of the Cr-rich (α_2) phase much more sensitive to changes in the aging temperature than the Fe-Co rich (α_1) phase. The σ phase field that is present in the Fe-Cr-Co ternary phase diagram extends across the diagram from the Fe-Cr binary to the Cr-Co binary. Williams and Paxton (24) and Williams (25) first proposed the presence of the miscibility gap below about 520 C. This requires an ($\alpha+\alpha'$) eutectoid reaction at this temperature, however, there is some discrepency about this reaction (37). In any event, reactions involving σ are always sluggish at these reduced temperatures. The σ phase has a tetragonal unit cell with 30 atoms per unit cell and in general has c/a ~ 0.52. There is evidence for an order-disorder transformation within the σ phase which may account for the very high hardness and brittleness of the σ phase. Commercial steels containing Cr are often susceptible to σ formation after prolonged aging at temperatures of 650-900°C. The phase transformation occurs by a nucleation and growth mechanism without gross diffusion (13). Due to the sluggish growth kinetics the σ phase forms heterogeneously at grain boundaries. This precipitation deteriorates the mechanical properties, particularly

the impact toughness. Sigma phase has been observed at the grain boundaries in the Fe-Cr-Co alloys (14). The phase is nonmagnetic at room temperature (38), however, it has only a slight effect on the magnetic properties because the volume fraction present is generally rather small.

The mechanical hardening of the Fe-Cr-Co alloys will certainly be tied to the magnetic hardening, in that both are greatly affected by microstructures following spinodal decomposition. The theory of spinodal decomposition is well understood (39,40) and much work on characterizing its effects on the mechanical properties (5-11) as well as magnetic properties (14-18) has been done. In general, the yield strength is proportional to the difference in lattice parameter δa (therefore the composition) between the two decomposed phases and nearly independent of both the spinodal wavelength (λ) and the relative volume fraction of the two phases (8-11). Dahlgren (8) has proposed a model that predicts the yield stress of the aged material by performing a calculation of the internal coherency strain. The model shows that correct dependence on the lattice parameter differences and has shown good agreement with the Cu-Ni-Fe spinodal alloys (8,11).

Because the origin of the miscibility gap in the Fe-Cr-Co alloys lies in the Fe-Cr binary system, it is important to be aware of the mechanical properties of these alloys. As mentioned earlier, the first evidence of a phase transformation in Fe-Cr alloys at low temperatures was from mechanical hardening. The mechanical hardening is quite remarkable; in fact, there can be greater than a two fold increase in the diamond pyramid hardness (e.g. ref. 41). Unfortunately, associated with this increase in hardness is the onset of severe embrittlement. This embrittlement has come to be known at "475°C embrittlment", since,

most of the work has been done at this temperature. Several explanations as to the nature of the embrittlement have been put forth (12,42) but it is generally accepted that the ultimate reason for the embrittlement lies in the decomposition that takes place at 475°C. Two important contributions to the embrittlement are an increase in the yield stress, which impedes the relaxation of stress concentrations, and the change to twinning as the major mode of deformation (12). In addition, it was observed that the yield and fracture stresses have a grain size dependence. The smaller grain sized material tends to increase the ductility of the Fe-Cr alloys and shifts the brittle-transition to longer aging times. Deformation prior to aging was also found to improve the ductility slightly (12).

The precipitation hardening in high strength stainless steels has been investigated by Coutsouradis et al. (43) and Abson and Whiteman (44). In either case, the yield strength, UTS, and Vickers hardness were observed to improve with aging, greater hardening occurred at lower aging temperatures. The alloys containing more Co showed better hardening but exhibited poorer ductility and impact toughness. After aging at 500°C a finely dispersed precipitate was observed.

III. ALLOY SOLUTION

Four alloys were chosen for examination in this study, two are ternary alloys and two have alloying additions of V and Ti. The nominal compositions are: Alloy A: Fe (balance) - 28Cr-15Co (w+.Z), Alloy B: Fe (balance) - 23Cr-15Co-5V (w+Z), Alloy C: Fe (balance) - 23Cr-15Co-3V-2Ti (w+Z), and Alloy D: Fe (balance) - 31Cr-23Co (w+Z). Alloy D was selected for the study because it was one of the first alloys found to have excellent magnetic properties and is ductile before magnetic aging (1). The microstructure of this alloy has since been characterized in great detail (14). It is always desirable to reduce the amount of alloying elements required; alloy A was selected to show this effect. The Bell Laboratory's alloy "Chromindur" is based on this alloy (2) and the alloy has been extensively studied by Belli (17). An added benefit of reducing the Chromium content is a reduced likelihood of forming a sigma phase. Additions of V and Ti were made to this base alloy to further reduce the Chromium and to alter the decomposition kinetics which allows for a less severe quenching requirement (35). In general the alloys were selected to represent a variety of Fe-Cr-Co alloys that may find possible commercial acceptance.

IV. EXPERIMENTAL PROCEDURE

A. Materials Fabrication and Treatment

Four alloys were chosen for use during this study, two are ternary alloys and two have alloying additions of V and Ti. The base alloys: Alloy A, Fe(balance)-28Cr-15Co (wt%) was selected because of its excellent magnetic properties (35) and its promise of becoming a commercially important alloy. The additions of V and Ti are suggested by the phase diagrams shown in Fig. 4 and 5. In these alloys 5 wt% Cr is replaced with either V or V + Ti; the compositions are: Alloy B, Fe(balance-23Cr-15Co-5V (wt%) and Alloy C, Fe(balance)-23Cr-15Co-3V-2Ti (wt%). Another alloy, Alloy D, Fe(balance)-31Cr-23Co (wt%) was investigated in order to compliment the rather detailed work on the alloys magnetic properties (14). To aid as a deoxidizer 0.5 wt% Mn was added to each melt.

Chemical analysis verified the chemical composition to be within 1% of the intended compositions. The major impurity was found to be nitrogen, only small amounts of carbon were present. Typical values found were:

	Alloy A	Alloy B
Carbon:	< 0.001%	< 0.001%
Nitrogen:	0.018%	0.010%

The ingots were vacuum melted and chill cast into copper molds to avoid segregation. Alloys A and D were homogenized at 1350°C and alloys B and C were homogenized at 1000°C for 2 days. After homogenization, the ingots were hot rolled using a square bar mill and swaged at room temperature to the appropriate finished diameter.

Prior to aging, the alloys were solution treated at 1300°C (alloys A and D) and 1000°C (alloys B and C) for 1 hour in an Argon atmosphere.

Isothermal aging was done at either 640°C or 600°C for various times. To take advantage of the rapid kinetics of spinodal decomposition at high aging temperatures and the large difference in composition of the two spinodally decomposed phases at low aging temperatures, the method of step aging has been employed. This technique has shown success in improving both mechanical properties (11) and magnetic properties (14, 17) of spinodally decomposed alloys. A schematic diagram of the aging sequence used for alloys B and D are shown in Fig. 7 and 8 respectively. A thermal-mechanical treatment was used on alloy B which utilized both cold work and isothermal aging. In this treatment the material was solution treated, swaged at room temperature to a reduction of 50% in cross-section area and subsequently isothermally aged.

B. Mechanical Testing

Tensile properties were measured from round tensile bars whose dimensions are shown in Fig. 9. The tensile bars are proportional to ASTM standard tensile bars (ASTM E8-79) except that the gage length was reduced to 22.23mm (0.875in) in order to economize material. The specimens were finish-machined between the solution treating and the final aging treatment. The tests were performed on an MTS testing machine. Two specimens were treated at room temperature for all aging conditions. The specimens were pulled at a constant rate of 0.06 cm/min. The yield strength was measured at 0.2% offset, the total elongation was measured from the change in the gage length, and the uniform elongation was measured from the load-deflection curve.

The microhardness was measured from specimens taken from the grip areas of the tensile specimens. The measurements were made on mounted and polished specimens. Rockwell hardness measurements were made on polished slices of the ingots. Since some of the aged materials were

embrittled and failed before yielding in tension, hardness provides consistent basis for evaluating hardening.

The specimen design used for the Charpy impact testing is sketched in Fig. 10 and conforms to ASTM standards (ASTM E23-72). The tests were done at room temperature using a 232 ft-lb (315J) capacity testing machine.

Flat plate bend tests were performed on specimens 2 in x 0.40 in x 0.030 in (51 mm x 10 mm x 0.76 mm). A three point bend test fixture was used that allowed for approximately a 100° bend angle and the bending radius was four times the specimen thickness.

C. Microscopy

Light optical metallography was performed on samples taken from the grip areas of the tensile specimens. The specimens were mounted and both electro-chemically polished (electrolyte: 23% perchloric acid, 77% acetic acid; 10V) and etched (etchant either Kallings reagent (45) or 5% oxylic acid in water at ~1-5V). All light optical metallographic work was done on a Ziess Ultrophot II optical metallograph. An oil immersion lens was used for high magnification work.

Specimens for electron microscopy were sliced from the grip areas of the tensile specimens. The material was thinned to less than 5 mils by mechanical polishing. Discs 3 mm in diameter were then spark eroded and jet polished in a 23% perchloric acid-77% acetic acid solution. The optimal thinning condition was at 10V and 38-40 mA. The specimens were examined in a Philips EM301 electron microscope operating at 100 kV.

The investigation of the fracture surfaces was performed on an ARM1000 scanning electron microscope operating at 20 kV. The SEM instrument was also equipped with an EDAX X-ray energy spectrometer enabling localized chemical analysis.

V. EXPERIMENTAL RESULTS

A. Spinodal Decomposition

An example of the microstructure of as-quenched alloy B is shown in Fig. 11. The quench was rapid enough to suppress any decomposition.

The evolution of the spinodally decomposed microstructure for isothermal aging is shown for alloys A and B in Figs. 12 and 13 respectively. In each case Figs. A-C are for 600°C aging and D-F are for 640°C aging and the α_1 and α_2 phases correspond to the light and dark contrast respectively. The microstructures are typical of those found for other Fe-Cr-Co alloys (14, 17). The early stages of decomposition proceeds in a very isotropic fashion, but as coarsening occurs the decomposition products tend to align themselves along $\langle 100 \rangle$ directions. This is a consequence of reducing strain energy (9), since $\langle 100 \rangle$ directions are the elastically soft directions. The amount of strain created by decomposition must necessarily be small. This suggests that the difference in lattice parameter between the two decomposing phases is small. The difference in lattice parameter in an aged Fe-Cr-Co alloy has been measured to be less than 1% by the method of high resolution lattice imaging (14).

The coarsening rate of either alloy is significantly higher when aged at 640°C then when aged at 600°C. Figs. 14 and 15 illustrate the growth of the average wavelength as a function of aging time. The coarsening rates of each alloy at either aging temperature are essentially linear over the range shown. The coarsening rates are nearly the same for either alloy when aged at the same temperature.

Spinodal alloys are known to maintain a relatively constant

wavelength when aged by the step aging technique (11). However, as the wavelength remains fairly constant, the composition of the decomposing phases changes as dictated by the appropriate pseudo-binary tie line (11). Fig. 16 shows the similarity between the microstructure found in alloy D after aging steps 2 and 4 respectively. As expected the wavelength shows little change between the two aging steps. The wavelength after step 2 is 235Å whereas the wavelength after step 4 is only 270Å, an increase of 16%. The volume fraction of the α_1 phase (light contrast) increases slightly from 45% to 55%. For either aging condition, decomposition is quite isotropic and there appears to be a large amount of connectivity within a single phase. Even though the wavelength and volume fraction do not change appreciably, a considerable change in composition can occur which could have a significant effect on the mechanical properties.

B. Grain Boundaries

Grain boundaries, have a major effect on the properties of polycrystalline materials (51). For the material used in this study the two most important characteristics of the grain boundaries are: 1) mobility of the grain boundaries at elevated temperatures and 2) the formation of a grain boundary phase. The importance of the grain boundary mobility lies in determining the final grain size of the material. A representative optical micrograph of alloy A is shown in Fig. 17a. Fig. 17b is an enlargement showing possible evidence of a grain boundary being pinned by an inclusion. The average grain size of the material is measured to be approximately 650 μm. Figs. 18a and 18b are from alloy B; in this case the grain size is measured to be only 70 μm. This large difference in grain size can be attributed to two primary factors.

First, a lower homogenization and solution treating tempertature could be used because the addition of V reduces the size of the γ-loop (Fig. 4). Second, inclusions may pin grain boundaries, which slow the rate of grain growth. The effectiveness of pinning sites depends upon the size and distribution of the inclusions. The effects of these two factors are shown in Figs. 17 and 18. Alloy A (Fig. 17) has grain boundaries that are straight, with the exception of some grain boundaries being pinned by inclusions. The inclusions are approximately 1 μm in diameter and 30-40 μm apart. Alloy B (Fig. 18) has a quite different grain boundary morphology. The grain boundaries are more curved, with numerous grain boundaries being pinned by inclusions and many triple point grain junctions are far from the equilibrium 120° configuration. The inclusions in alloy B are smaller (0.25 μm) and more closely spaced (~ 10 μm) and can serve as better pinning sites. The TEM micrographs in Figs. 19 and 20 taken from alloy B, clearly show that the inclusions can be effective grain boundary pinning sites. The SEM microchemical analysis (see Fig. 21, lower x-ray spectrum) shows the inclusion to be almost entirely Cr.

Since the x-ray analysis cannot detect light elements, such as nitrogen and carbon, the actual composition may not be pure Cr. In fact, noting the high nitrogen impurity content (0.018 wt.% N) the inclusion may very likely be a Cr_2N compound. The volume fraction was too small to detect such a compound with x-ray diffractic However, without further evidence (e.g., electron microdiffraction, electron energy loss spectroscopy) this would be only speculative. Unfortunately, due to the size and distribution of the inclusion, it was not possible to locate these regions for TEM observation.

Formation of a grain boundary phase is the second major feature affecting the material's mechanical properties. Figure 22 is an SEM micrograph of a round bar of alloy A that was aged at 640°C for 1 hr and swaged (reduction in area ~20%). Clearly, intergranular failure has occurred, but equally noticeable is the ductility of the matrix material. The presence of the grain boundary phase is very apparent in Fig. 23. This optical micrograph is of alloy D aged by step aging. Figure 23 is after step 3 (600°C) and Fig. 23 is after step 4 (580°C). The grain boundary phase is quite thick, in fact, it has begun growing from the grain boundaries, consuming the matrix material. The grain boundary phase grows the fastest in alloy D which is attributed to the higher Cr content of the alloy. Figure 21 is a typical grain boundary of alloy A aged at 600°C for 1 hr. Figure 21 is a SEM micrograph of a similar grain boundary. Three separate areas were chosen for EDX microchemical analysis (special resolution ~1 μm^2). In order to make a meaningful comparison, the same take off angle and same collection time were used for each area. The top x-ray spectrum in Fig. 21 is a comparison of the grain boundary composition (bars) with the matrix composition (dots). There is a shift in the peak heights in both the Cr peak and the Fe peak due to a change in composition. Due to the thinness of the grain boundary phase, this is only an indication of a change in composition at the grain boundary. However, this indicates the grain boundary phase to be Cr enriched and a sigma phase may be present.

The series of TEM micrographs in Fig. 24 show a grain boundary with the grain boundary phase present. The material shown is alloy A aged at 640°C for 100 hr, causing considerable thickening of the grain boundary phase. Figure 24a and b are TEM bright field and dark field

images respectively and Fig. 24c is an SAD of the grain boundary area. The diffraction pattern is indexed to show the (120) bcc matrix pattern superimposed with several (100) sigma patterns. The matrix pattern serves as an internal calibration of the microscope camera constant to assure the highest possible accuracy in identifying the grain boundary phase. The measured values for the lattice parameters are a_o = 8.74Å and c_o = 4.38Å with a c/a ratio = 0.50. Typical values for the Fe-Cr sigma phase (13) are a_o = 8.7995Å and c_o = 4.5412Å with a c/a = 0.516. These are in good agreement and of course the lattice parameter is expected to change slightly with the addition of Cobalt. The diffraction pattern appears to be quite complicated but it can be very easily understood. There is the bcc matrix pattern plus the main (100) sigma patterns labeled (i). Many of the extra spots are caused by double diffractions and the pattern labeled (ii) illustrates this. Other spots are due to another sigma particle being included within the intermediate aperture. This grain is misoriented by approximately 2^o.

Sigma is known to be a hard brittle phase that preferentially forms at the grain boundaries and which often leads to the deterioration of the mechanical properties, particularly the impact toughness (13). Commercial alloys containing more thar approximately 16 wt% Cr are susceptible to σ phase formation when held at temperatures of 650-900^{o}C for prolonged periods of time (13). Furthermore, the higher the Cr content, the more rapid is the formation of σ. Even though the σ phase forms primarily at the grain boundaries, it is not necessarily a continuous film. In fact, the morphology of the grain boundary phase appears to be very dependent upon the degree of misorientation of the

adjacent grains. Figure 25 is a TEM bright field-dark field pair of alloy A aged at 600°C for 1 hr; it shows the reversal of contrast associated with the grain boundary phase. The grain boundary is very nearly edge on so that the thickness of the grain boundary phase is only a few hundred angstroms. The σ phase coats the grain boundary quite uniformly but is not as a continuous film. Aging the material 5 hrs at 600°C causes some coarsening of the σ as shown in Fig. 26. Note that the σ is starting to grow into globular particles which is more evident in Fig. 27. Figure 27 is from alloy A aged at 640°C for 10 hrs and shows a more advanced stage of coarsening. Clearly the σ phase is not continuous but consists of particles of the order of 1000Å in size.

The morphology of the grain boundary precipitation depends on the grain boundary structure and is not just a function of the aging time and temperature. As an example, Fig. 28 shows two grain boundaries observed in alloy B. Figures 28a and b are taken from the material aged for 1 hr at 600°C whereas Figs. 28c and d are after aging 100 hrs at 600°C. The resemblance is quite remarkable; the grain boundary phase is not continuous and the particles are of similar size. Sigma is known to have rather slow growth kinetics and these micrographs certainly bear this out. However, this is not the complete picture. Figure 29 illustrates how varied the morphology of the σ phase can be. Figure 29 is a micrograph of alloy B aged again at 600°C for 100 hrs. Shown is a triple point junction and the diffraction patterns of the three grains are shown to indicate the degree of relative misorientation. The growth of the σ is most prominent at the triple point but also the growth between grains A and B and grains A and C has been quite substantial. The growth between grains B and C in comparison has been

very slow. The diffraction patterns indicate that the misorientation between grains B and C is quite small; both grains are tilted from a (111) orientation but A and B and A and C are misoriented on the order of 40°. Aging the alloy at 640°C produces similar results. Figure 30 shows a triple point after aging alloy B for 1 hr. Virtually no σ phase was observed. However, aging for 10 hrs produced σ at triple points and along the grain boundaries but again not in a continuous fashion (see Fig. 31). This orientation dependence of the grain boundary phase has been observed in other systems. A detailed analysis has been made by Gronsky (57) using the Aluminum-Zinc alloys.

C. Mechanical Properties

C.1. Isothermal Aging

The mechanical properties of alloy A, B, and C isothermally aged are summarized in Figs. 32-39. The three alloys in the as-quenched condition (i.e. prior to spinodal decomposition) were found to be ductile. Upon aging inside the miscibility gap, the alloys exhibit an age hardening response similar to that often found in spinodal systems, i.e. higher tensile strengths were associated with low aging temperature and accompanying the higher strengths was a decrease in ductility.

C.1.1. Alloy A Fe-28Cr-15Co

In the as-quenched condition, alloy A has a yield stress of 55.8 ksi (385 MPa) with a uniform elongation of 9.4%. For the material aged at 640°C, Fig. 32 shows an increase in the yield stress to a peak of approximately 75 ksi (518 MPa) with no change in the uniform elongation and a slight drop in the total elongation. (In Fig. 32, the solid symbols refer to uniform elongation, the open symbols

refer to total elongation, and the half-filled symbols refer to the uniform and total elongations being equal.) However, aging at 600°C has a much different effect on the material. Aging at the lower temperature does produce a more significant increase in the strength. Unfortunately, associated with this increase in strength is a drastic drop in the ductility. In fact, aging only 5 min at 600°C produces a 30% increase in stress to fracture, but the material becomes sufficiently embrittled to cause failure before yielding could even begin.

The single crystal hardness, as measured by Vickers microhardness, is shown in Fig. 33. Microhardness is a convenient indication of the hardening because the triaxial state of stress allows deformation to take place even if the material is sufficiently embrittled to cause failure in tension before yielding. Therefore, a consistent comparison between the ductile and brittle material can be made. Aging at 640°C produces a hardness curve very similar to the one found in Fig. 32 for the tensile testing. In either case, the peak hardness occurs after aging for 5 hrs. The curves in Figs. 32 and 33 for aging at 600°C however, are quite dissimilar. The apparent tensile strength drops off after aging beyond 5 mins whereas, the microhardness increases until it reaches a peak VHN of 360 after 10 hrs aging.

The room temperature Charpy impact toughness of the isothermally aged alloy A is shown in Fig. 34. As might be expected, the 108 ft-lbs (146 J) energy absorbed during failure for the as-quenched material is quite high. However, the large drop in the impact toughness of the material aged at 640°C is larger than expected when considering the tensile elongations. But the extremely low values of the impact toughness of the material aged at 600°C is consistent with the

poor ductility observed during the tensile testing. After aging for 1 hour the impact energies were 12.9 ft-lbs (17 J) and 2.2 ft-lbs (3 J) for 640°C and 600°C aging temperatures respectively, and the values decreased only slightly with aging time.

C.1.2. Alloy B Fe-23Cr-15Co-5V

Replacing 5% Cr with 5% V altered the hardening and subsequent embrittlement in a very significant manner. The variation in yield stress with isothermal aging time is shown in Fig. 35. In the as-quenched condition, alloy B has a yield stress considerably higher than that found for alloy A, i.e., 70.4 ksi (485 MPa) as opposed to 55.8 ksi (385 MPa) measured for alloys B and A respectively. The single crystal microhardness likewise, reflects this increase in hardness in the as-quenched condition. alloy A has a microhardness of 203 kg/mm^2 whereas alloy B showed an increase to 214 kg/mm^2. This indicates that replacing 5 wt% Cr with 5 wt% V has led to some solid solution hardening, since from the microscopic evidence the quench appeared rapid enough to maintain the high temperature supersaturated solution. The increase in strength due to solid solution hardening may be amplified by the smaller grain size of alloy B. Because the heat treatments used in this study were designed to be consistent with those used in developing optimum magnetic properties, a significant difference in grain size exists between alloys A and B. The strength of BCC materials is known to be particularly sensitive to grain size (46) and this may account for some of the large variation in yield stress. Lagneborg (12), in his work with Fe-Cr alloys, observed a strong grain size dependence on both the yield and fracture stress that followed a $(d)^{-\frac{1}{2}}$ relationship, where d is the average grain diameter.

Aging alloy B at 640°C produces a very mild degree of hardening, which peaks at 77.7 ksi (536 MPa) after aging 1 hr with little change in the uniform elongation. The onset of the embrittlement of alloy B, when aged at 600°C, occurs at much longer times than in the case of alloy A. Aging alloy B at 600°C for 20 min increases the yield stress over 40% above that of the single phase material with only a drop in the uniform elongation to 9.9% from 12%. After aging 1 hr at 600°C, necking no longer occurs, but it is not until aging 100 hrs that all plasticity is lost and the material fails before yielding. This is a considerable improvement over alloy A, since alloy A failed before yielding for aging times 5 min and longer when aged at 600°C. In addition alloy B shows no drop off in the fracture stress, even after being embrittled, quite the opposite to that of alloy A.

The microhardness of alloy B as a function of aging time (shown in Fig. 36) shows again the normal age hardening characteristics. Aging at 640°C produces only a small amount of hardening that peaks after 1 hr and decreases slightly for all further aging. Due to the lower aging temperature of 600°C, the hardening is greater. Again the hardness peaks after aging 1 hr. The hardness of alloy B peaks much quicker than alloy A, 1 hr as opposed to approximately 10 hrs. The maximum hardness of alloy B is greater than that of alloy A when aged at 640°C, but the reverse is true when the material is aged at 600°C.

The Charpy impact toughness for the as-quenched alloy B is quite high, (Fig. 37) 60 ft-lbs (81 J), but is not as high as that measured for alloy A. Similar to alloy A though, is the rapid and severe drop in the impact energy upon aging, which is clearly indicated in Fig. 37.

C1.1.3. Alloy C Fe-23Cr-15Co-V-2Ti

The addition of V + Ti improves the mechanical properties when compared to the ternary alloy A but is not as effective in retarding the embrittlement as just the addition of V (alloy B). The yield stress of the as-quenched alloy C is 58.3 ksi (402 MPa) (Fig. 38). This is similar to that measured for alloy A but less than that found for alloy B. The material also showed excellent uniform elongation with a value of 14.7%, better than either alloy A or B. Fig. 38 shows the variation of strength and elongation with aging time and temperature. The material aged at 640°C becomes harder with aging time, but unlike alloys A and B, the increase in strength does not peak at 1 hr but continued to increase up to 100 hrs. The highest value measured was 79.0 ksi (545 MPa), after aging 100 hrs. However, ductility was sufficiently reduced to cause failure before the onset of necking in this specimen. Aging at 600°C produced a fairly flat response in the fracture stress, and it was not until aging 1 hr that the material failed prior to yielding. Unlike alloys A and B, aging alloy C 100 hrs caused a significant increase in the strength. Fig. 39 shows the variation in Vickers microhardness with aging time and temperature. The as-quenched material was slightly harder than alloy B. Hardening when aged at 640°C was very slight; however, at 600°C hardening continued through the entire 100 hrs of aging.

Limited Charpy testing showed the material to be embrittled similar to alloys A and B.

C.2. Step Aging

In order to achieve the high strengths associated with low temperature aging yet take advantage of the rapid decomposition

kinetics associated with high temperature aging, the method of step aging was employed. Alloys A, B, and C were aged using the step aging techniques shown in Fig. 7. Figures 40, 41, and 42 show the variation in hardness throughout the aging sequence. The Rockwell "C" hardness indicates the hardness averaged over several grains whereas the Vickers microhardness is the hardness of single grains, eliminating the effect of grain boundaries. Previous work on Cu-Ni-Fe (11) alloys showed that the hardening due to step aging was mostly controlled by the final aging temperature. This also appears to be the case for the Fe-Cr-Co alloys. The hardness increased incrementally as each lower aging temperature was used. The three alloys typically increase from approximately R_C10 to greater than R_C35 and the microhardness parallels this increase closely as in Figs. 40 and 41.

Since the mechanical properties of alloy B, as illustrated in the previous section, are superior to either alloys A or C, the tensile properties of alloy B were measured after being heat treated using the step aging technique (see Fig. 7). Figure 43 shows the variation in strength with aging step. The increase in the strength is similar to the increase in hardness shown in Fig. 41. The elongation drops as the strength is increased; however, it is not until step 5 (580^{o}C aging temperature) that virtually all ductility is lost. Supporting the theory (11) that the final aging temperature, i.e. the composition, determines the strength, step 4 corresponds to aging at 600^{o}C and has a yield strength of 105 ksi (724 MPa) which compares quite well with the value obtained by isothermal aging at 600^{o}C. Figure 37 shows the Charpy impact toughness after step 1 (as-quenched), step 4 (600^{o}C), and step 7 (540^{o}C). As with the isothermally aged material, the

reduction in the impact toughness is quite remarkable. Aging to step 4 exhibits a uniform elongation of nearly 8%, yet the impact toughness is only 4 ft-lbs (5 J). After step 7, when the material fails before yielding, the toughness is 1.5 ft lbs (2 J). Clearly the material has been severely embrittled.

The step aging treatment of Fig. 8 has been applied to alloy D, which has received much attention in regard to its magnetic properties (14). Figure 44 shows the variation in strength, microhardness, and coercive force with aging steps. The shape of the curves of the coercive force and the microhardness are quite similar. This is to be expected, since the coercive force is a measure of the resistance to moving domain boundaries whereas the hardness is a measure of the resistance to plastic flow. Both of these properties are influenced by the strength of obstacles, and necessarily become higher as lower aging temperatures are used. The strength does not follow this trend because the embrittlement of the material does not allow the possible increase in strength to be realized.

C.3. Thermo-Mechanical-Treatment (TMT)

One technique successfully used in retarding embrittlement, particularly at the grain boundaries, in spinodally decomposed materials is a thermomechanical treatment (47). Figure 45 shows the variation in strength with aging time of the TMT material and is compared with the purely thermal treatments. Indeed the TMT retards the onset of embrittlement. After 10 hrs aging at 600^{o}C there is 10% total elongation compared to 1% for the purely thermal treatment. The strength of the material is determined by the high level of work hardening instead of age hardening. The yield stress

of the as-rolled material is almost twice that of the material prior to rolling. The high strength level persists throughout the isothermal aging treatments whereas the isothermally aged material produces the standard age hardening characteristics. Figure 46 shows typical stress-strain curves for the as-rolled (a), 1 hr aging (b), and 100 hr (c) aging conditions. The as-rolled material begins necking virtually at the yield point. This feature is also observed in highly deformed materials, such as in explosive loading (48, 49) and is referred to as work softening. After aging 1 hr at 600°C, some annealing occurs, as seen by some work hardening in Fig. 46b. However, the yield stress does not appreciably drop, indicating that most of the work hardening has remained. After aging 100 hrs the material is embrittled; yet, the material does show yielding, which is significantly above the yield for the purely thermal treatment.

D. Fractography

D.1. Isothermal Aging

D.1.1. Alloy A

The SEM micrographs of the fracture surfaces of alloy A when tested in tension are shown in Fig. 47. The as-quenched material shows the dimpled rupture fracture surface associated with a ductile mode of failure. The fracture surfaces of the material aged at 640°C clearly shows the material to be embrittled, particularly the grain boundaries. The strength of many grain boundaries has been sufficiently reduced so as to cause them to separate; yet, not all grain boundaries were weakened, since complete intergranular failure was not observed. In fact, many grains were observed to individually neck and fail in a ductile dimpled rupture fashion (see Fig. 47).

The mode of failure is not significantly affected by continued aging once the onset of embrittlement occurs.

The material aged at 600°C also exhibits evidence of embrittlement, though in this case, both the grain boundaries and the matrix material are affected. Figure 47 illustrates the consequence of the embrittlement upon the mode of failure when pulled in tension. Aging only 20 min at 600°C causes failure to occur through a mixture of quasi-cleavage and intergranular failure. After aging 10 hrs the typical river pattern associated with cleavage steps are present. Also observed are areas of feathered tongues which are shown in detail in Fig. 48. Tongues are generally associated with fracture along microtwins that were formed by plastic deformation in front of the propagating crack tip (50). This tends to indicate that twinning may become an important mode of deformation when the material is aged at 600°C. This could contribute to the loss of ductility; since twinning is much less effective than slip in accommodating plastic deformation. Confirmation of twinning deformation has been obtained (see Fig. 60).

The fracture surfaces of the Charpy V-Notch specimens of alloy A aged for various times at both 600°C and 640°C are shown in Fig. 49. The material in the as-quenched condition failed primarily by dimpled rupture. The ductile nature of the failure is expected due to the large amount of impact energy absorbed. The fracture surfaces of the material aged at either 600°C or 640°C showed severe embrittlement. The material aged at 600°C showed a mixture of intergranular failure and transgranular cleavage, similar to that found for the material tested in tension. After aging for 1 hr at 600°C, Fig. 49 shows smooth flat grain boundaries that had failed, along with secondary

cracking that appears to follow grain boundaries.

Unlike the material aged at 640°C and tested in tension, the material aged at 640°C and impact tested shows evidence of both grain boundary and matrix embrittlement. The mode of fracture, once the embrittlement occurs, does not change with aging time.

D.1.2. Alloy B

The results of the failure analysis of alloy B (shown in Fig. 50 for the tensile test specimens and Fig. 51 for the Charpy impact specimens) are very similar to the results of alloy A, except that the onset of embrittlement was significantly retarded. Whereas alloy A, aged at 600°C for 5 min, failed in tension in a completely brittle manner, alloy B remained completely ductile after 20 min. Aging for 1 hr and longer showed evidence of cleavage, yet the amount of grain boundary failure appears to be small. Also present are secondary cracks, indicating that crack propagation normal to the direction of the primary crack growth had occurred. Fig. 52 shows a detail of a fracture surface from alloy B aged at 600°C for 10 hrs. Numerous well-defined feathered tongues are present (e.g. see arrow) similar to those found with alloy A. Again, these are generally associated with microtwinning.

Aging at 640°C shows basically the same characteristics as those found for alloy A, but the rate at which the embrittlement occurs is reduced. As seen in Fig. 50 aging 10 hrs at 640°C embrittles a few grain boundaries and after 100 hrs many grain boundaries are embrittled. As found for alloy A, the individual grains remain ductile, necking of individual grains and dimpled rupture fracture surfaces are observed.

The fracture surfaces of the Charpy impact specimens (see Fig. 51) show the as-quenched material to be primarily ductile, with some

areas of cleavage and some secondary cracking. Aging at either 640°C or 600°C has embrittled the material, as evidenced by the drastic drop in Charpy toughness (Fig. 37), and the mode of failure is shown in Fig. 51. Alloy B aged at 640°C shows some small areas of dimpled rupture, even though the impact toughness values are very low. The amount of grain boundary failure for aging at either 640°C or 600°C is considerably less than that found for alloy A. There is also a considerable amount of secondary cracking present.

D.1.3. Alloy C

Alloy C, when pulled in tension, showed characteristics very similar to those observed for alloy B and are illustrated in Fig. 53. The as-quenched material exhibits a dimpled rupture fracture surface, indicating the ductile nature of the material when pulled in tension. When aged at 640°C, the matrix material remains ductile for the most part, except for some grain boundary failure. The material is embrittled very severely when aged at 600°C similar to both alloys A and B.

Charpy impact toughness specimens failed by cleavage for either 640°C or 600°C aging very similar to alloys A and B.

D.2. Step Aging

Figure 54 shows the fracture surfaces of alloys B and D when pulled in tension and after various stages of the step aging sequence. Figure 54a and b are from alloy D after step 2 (640°C) and step 4 (600°C) respectively, and Fig. 54c and d are from alloy B after step 4 (600°C) and step 5 (580°C) respectively. Figure 54a shows a mixed mode of failure; dimpled rupture, cleavage, and intergranular failure can be observed, but the material showed necking and

good tensile elongation. Further aging to step 4 changed the failure to a cleavage mode with evidence of secondary cracking. The mechanical properties (Fig. 44) indicate embrittlement at this stage. This type of failure prevailed throughout all subsequent aging treatments.

Alloy B, spinodally decomposed by step aging, shows results similar to those of alloy D. High temperature aging produced a mixture of both ductile and brittle failure, whereas low temperature aging showed only brittle failure. Fig. 54c illustrates the mixture of ductile and brittle fracture surfaces observed from the alloy aged through step 4 and pulled in tension. Reducing the aging temperature by only 20°C to 580°C (step 5) severely reduces the materials ductility (see Fig. 22) and causes the material to fail by pure quasi-cleavage as is shown in Fig. 54d.

Charpy impact specimens of alloy B (Figs. 55a and b correspond to steps 4 and 7 respectively) show that brittle failure occurred after both high and low temperature aging. This is consistent with that found for the isothermally aged material.

D.3. Thermo-Mechanical-Treatment (TMT)

The TMT did not appreciably affect the failure mode of alloy B. As for the isothermally aged material, the fracture surface after 20 min. aging at 600°C for both isothermal aging and TMT (shown in Fig. 50 and 56a respectively) was primarily dimpled rupture. The TMT did, however, tend to increase the amount of grain boundary failure. Continued aging a 600°C eventually embrittled the material. Fig. 56b shows the fracture surface after aging 10 hours. Even though failure was by cleavage and the fracture surface looks very similar to the case of isothermally aged material (see Fig. 50) the tensile properties were far superior for the TMT material (Fig. 45).

VI. DISCUSSION

A. Age Hardening

Age hardening in the Fe-Cr alloys is explained by a mechanism consisting of both an athermal (temperature independent) and a thermal (temperature dependent) contribution. The temperature independent part consists of two mechanisms, one based upon the elastic interaction between dislocations and the precipitates (26) and the other based upon the difference in elastic modulii for the precipitate and the matrix (53). The temperature dependent part of the hardening is mainly determined by a process where the thermal barriers are represented by the energy corresponding to the breaking of chemical bonds when a dislocation intersects a Cr-rich precipitate particle (52). In the alloy Fe-30Cr aged at 475°C, the hardening produced an increase of 64 ksi (441 MPa) to approximately 120 ksi (827 MPa) when tested at room temperature (52). It was also determined that the athermal part of the strengthening accounted for 78% of the hardening while the thermal part contributed only 22%.

The calculation based on the internal coherency strains that has been successfully applied to several spinodal alloys (8,11) requires a two phase microstructure of coherent parallel lamellae with different lattice parameters in each phase. This creates a state of biaxial stress in the lamellae. Unfortunately, the Fe-Cr microstructure does not fit this model since the precipitates are essentially spherical.

Age hardening in the Fe-Cr-Co alloys appears to be similar to that found for the Fe-Cr alloys. Verification of this by calculation is difficult because the elastic modulii of the decomposed phases are not known. Qualitatively however, the mechanisms can be justified. The mechanisms suggest that hardening improves with lower aging

temperatures, as is the case of the Fe–Cr–Co alloys. The composition of the α_1 and α_2 phases is further enriched in Fe–Co and Cr respectively and the difference in lattice parameter between the two phases increases as the aging temperature is reduced. The elastic moduli of the two phases will be more dissimilar with lower aging temperatures because the elastic constants are material properties and by changing the aging temperature the compositions of the decomposed phases change (e.g.the shear modulus, G, is to a first approximation a linear function of composition). Therefore the larger the difference in lattice parameter between the α_1 and α_2 phases, the greater the strain will be at the interface. This will cause a greater interaction with dislocations at the interface resulting in enhanced hardening. The interaction between dislocations and the α_1 - α_2 interface is illustrated in the TEM micrograph Fig. 57 (alloy A aged at 640°C for 100 hrs). The dislocations are held in the interface looping around the particles, giving the appearance of Orowan type hardening. The areas of bright contrast are caused by a g diffracted beam being included in the objective aperture.

An improvement in the hardening can also occur by improving the thermal contribution. Binary Fe-Cr alloys show pronounced solid solution hardening (54). The effects of composition on the solid solution hardening of the Fe–Cr binary is shown in Fig. 58 (taken from ref. 55), the solvent is Cr and solute is either Fe or Co. Lagneborg (52) has attributed the hardening to an increase in the lattice friction caused by a Peierls-Nabarro mechanism. It was suggested, based upon his experiments, that the net effect of alloying iron with chromium, with respect to the P-N mechanism, would be a more rigid lattice with slightly higher P-N barriers as compared to pure iron.

The solid solution hardening of the Fe-Cr-Co system, due to chromium concentration, has been studied. Six Cr-rich compositions were selected (see Fig. 59) that lie on the decomposed conjugate line passing through alloy A. Phase separation will occur along this line; therefore, the six compositions correspond to specific α_2 compositions associated with the appropriate aging temperature as dictated by the miscibility gap. Shown in Fig. 58 is the effect of the solid solution hardening of these six alloy compositions. The hardening due to $Fe_{0.79}Co_{0.21}$ as the solute is more pronounced than Fe but not as strong as Co. Again the Fe-Cr-Co system is very similar to the Fe-Cr system and the Peierls-Nabarro mechanism is likely to be operating.

Along with the solid solution hardening, the mode of deformation tends to become predominately twinning with increasing chromium content in Fe-Cr alloys (26). A very similar situation is observed in the Fe-Cr-Co alloys. Figure 60 shows a series of SEM micrographs of the severely deformed region in the vicinity of a Rockwell hardness indention. Figure 60a is of alloy #1 in Fig. 59 (pure Cr) which deformed only by slip. Twinning is found in Fig. 60b (alloy #2 in Fig. 59), and deformation is almost solely by twinning in Fig. 60c (alloy #4 in Fig. 59). The single phase alloy A (Fig. 60) deforms only by slip. This increase in twinning as the mode of deformation can lead to a reduction in ductility. This correlates with the evidence of microtwinning in the brittle fracture surfaces indicating that twinning may play an important role in the embrittlement of the aged Fe-Cr-Co alloys.

In contrast to the hard α_2 phase, the Fe-Co rich α_1 phase should be soft and quite ductile (56). Typically, the α_1 phase contains about 20% Co with very little Cr. At this Cobalt content ordering is unlikely, but more importantly, the critical temperature for ordering is below

570°C and that quenching in the disordered state is possible (56). Mechanical testing of an Fe-26 at .% Co alloy showed it to have a yield stress of 29 ksi (200 MPa) with an excess of 20% plastic strain to failure in the disordered state. Even in the fully ordered state the yield stress increased to 44 ksi (300 MPa) yet, had greater than 20% total elongation.

B. Matrix Embrittlement

The microstructure of the spinodally decomposed Fe-Cr-Co alloys has been shown to consist of a hard Cr-rich α_2 phase with a soft Fe-Co rich α_1 phase and the hardness of the α_2 phase appears to be the controlling factor in the age hardening of these alloys. However, the suggested hardening mechanism does not account for the severe matrix embrittlement that occurs when the material is aged at 600°C, while the matrix material is ductile when aged at 640°C. In an attempt to understand this effect, an experiment was devised to follow the ductility of the α_2 phase. The α_2 phase was singled out because as previously stated the Fe-Co rich α_1 phase is soft and ductile. The same material and process that was used for the hardness experiment was used for a three point bend experiment. The bend angle is a measure of the materials ductility, since the greater the bend angle, the greater the material may be plastically deformed. Figure 61 shows the results of the experiment, as before the solvent is Cr and the solute is $Fe_{0.79}Co_{0.21}$. The composition of the material has a strong influence on the ductility of the material.

The ductile-brittle transition, due to composition, occurs between alloys 3 and 5 with the inflection occuring approximately at alloy 4. When this is viewed in light of the location of the miscibility gap at 600° C and 640°C (see Fig. 59) the reason for the

large change in ductility when aged at 600°C becomes clear. The 620°C miscibility gap passes approximately through alloy 4. Therefore, any α_2 composition associated with higher aging temperatures will be more ductile than alloy 4, and any α_2 composition associated with lower aging temperatures will be less ductile than alloy 4. Aging at 640°C clearly creates a ductile α_2 phase and aging at 600°C creates a brittle α_2 phase.

In addition, the spinodal microstructures will enhance the embrittlement of the aged material. The microstructure consists of both a ductile and brittle phase when aged at 600°C, however, the material exhibits catastrophic failure. This means the ductile phase cannot arrest the crack propagation as might be expected. The inability to stop the crack propagation is a combination of two factors: the connectivity of the α_2 phase and the fine scale of the spinodal microstructure. The high degree of connectivity of the α_2 phase in effect make it a continuous phase whether it is the major phase or not. Once a crack begins to propagate, it can follow a path preferentially through the α_2 phase. Due to the proximity of each successive α_2 phase, the stress field preceding the tip of the crack may be great enough to initiate a crack in the next α_2 phase before the crack would actually reach the α_1 phase and become blunted.

Another microstructural feature that could lead to premature failure that is visible in Fig. 12c, is the rod-like nature of each phase. Because the rods show a great deal of connectivity, they take very irregular shapes. Where the rods are sharply bent a high stress concentration can result, which would directly contribute to deterioration of the fracture properties.

C. Grain Boundary Embrittlement

In addition to the matrix embrittlement that occurs with 600°C aging, severe grain boundary embrittlement has been observed after both 600°C and 640°C aging. The embrittlement is a consequence of a grain boundary phase and has been identified as σ-phase, in agreement with previous work on Fe-Cr-Co alloys (14). Sigma is known to be a hard and brittle phase and preferentially forms at grain boundaries. The formation of σ leads to deterioration of the mechanical properties and particularly the impact toughness. This was also found to be true in this work. Alloy B aged at 640°C serves as an example of the influence of the σ phase on the mechanical properties. Fig. 35 shows no drop in elongation even for long aging times yet Fig. 37 shows a very rapid and severe drop in Charpy impact toughness.

The morphology of the σ phase described previously indicates the σ precipitates preferentially along particular types of grain boundaries. This selective nature explains the fracture surfaces of the alloys aged at 640°C, Fig. 26, for example, shows alloy A aged at 640°C for 20 min. and 10 hrs. Many grain boundaries have clearly separated yet each grain apparently necked and failed instead of being pulled apart. This indicates some grain boundaries must be strong enough to withstand the applied load. These grain boundaries are most likely the grain boundaries without σ.

D. Comparison of Magnetic and Mechanical Properties

The methods of controlling magnetic properties are in principle very similar to those for controlling mechanical properties. Of the main parameters of interest in hard permanent magnets, only the saturation magnetization ($4\pi I_s$) is not structure sensitive and decomposition will have little effect on it. The other parameters

of general interest, the magnetic remanence (B_r) and the coercive force (H_c) are structure sensitive. The remanence is improved by a thermo-magnetic-treatment by elongating the magnetic Fe-Co phase in the direction of the applied field (14). The coercive force, however, depends upon the strength of a barrier to impede domain wall movement. This is improved by increasing the difference in composition between the two decomposing phases. Step aging has been found to be an effective method to increase H_c in Fe-Cr-Co alloys. (14, 17).

The mechanical age hardening of spinodal alloys is also structure sensitive. In this and previous work (11) the mechanical age hardening has been shown to be primarily a function of composition of the decomposing phases. Due to the embrittlement encountered with the Fe-Cr-Co alloys hardening was necessarily monitored by microhardness. In any event the magnetic parameter most similar to microhardness is clearly the coercive force. This is illustrated in Fig. 44. Both parameters are increased by lower temperature aging, which is expected.

Controlling magnetic properties is somewhat more difficult than the mechanical properties in spinodal systems, since the mechanical properties tend to be independent of morphology of their microstructure while the magnetic properties are not only sensitive to composition but to morphology also. Unfortunately one aspect of the mechanical properties that is a consequence of decomposition of Fe-Cr-Co alloys is the severe embrittlement. The alloy compositions required to produce good magnetic properties are destined to be brittle in the hardened condition. If a truly ductile hard magnet is desired, further alloy design is required to get away from the very brittle α_2 composition as illustrated in Fig. 61.

VII. SUMMARY AND CONCLUSIONS

The Fe-Cr-Co alloys used in this investigation all had similar basic characteristics. They all decompose by spinodal decomposition with resulting age hardening. Aging at high temperatures (e.g., 640°C) caused rather mild hardening and did not appreciably affect the tensile elongations. However, due to the formation of σ at the grain boundaries, the alloys are embrittled. The embrittlement is most noticeable with the drop in the Charpy impact toughness, which is similar to the σ embrittled stainless steels containing chromium. The σ forms preferentially at grain boundaries due to its sluggish growth kinetics. The morphology of the σ is very dependent upon the aging time and the character of the grain boundary, i.e., the degree of misorientation of the grains forming the grain boundary.

Low temperature aging had a much different effect on the alloys. Indeed the hardening at the low temperatures (e.g., 600°C) was far greater than had occurred with the high temperature aging. Unfortunately, with the low temperature aging not only was σ found at grain boundaries, but the matrix material was embrittled also. The tensile specimens typically failed with little or no plastic deformation in a brittle catastrophic fashion whereas the alloys aged at 640°C showed good matrix ductility. Due to the brittle nature of the aged material, tensile testing did not give an accurate representation of the age hardening response. Using microhardness the alloys aged at the lower temperature showed a considerable increase in hardness over the alloys aged at the higher temperature. This is in agreement with other work on spinodal alloys (11). The presence of σ at the grain boundaries only enhances the embrittlement at 600°C and this is again evident from the very low Charpy impact toughness values measured.

The method of step aging produces only a marginal effect on the morphology of the spinodal microstructure as the aging temperature is lowered, yet it greatly affects the composition of the decomposing phases. Measurements of the strength and hardness indicate that hardening improves with lower aging temperatures. However, ductility of the material is strongly influenced by the aging temperature. In fact changes of 20°C in the aging temperature have profound effects on the ductility. This implies that the ductility is independent of the spinodal morphology but strongly dependent upon the composition of the α_1 and α_2 phases.

The strong influence of the aging temperature on the ductility is due to the solid solution hardening of the α_2 (Cr rich) phase. The α_2 phase behaves similarly to both the Fe-Cr and Co-Cr binary systems in that the solid solution hardening can be quite remarkable. The peak hardness occurs at approximately 80% Cr, but associated with this hardening is a rapid drop in ductility. This shows that the composition of the α_2 phase is very critical with regard to ductility, since the aging temperature significantly affects the composition of the α_2 phase. In fact, aging at 640°C leaves a ductile α_2 phase while aging at 600°C leaves a brittle α_2 phase. One possible source of the embrittlement of the α_2 phase is the change from slip to twinning as the mode of deformation, which occurs with increasing amounts of chromium in the α_2 phase. This is reflected in the evidence of microtwinning in the cleavage faces of the fractured tensile specimens.

After embrittlement, alloy A shows a drop in the fracture stress, whereas alloys B and C show no drop. This is an effect of the large grain size associated with alloy A. Alloys B and C have a much

smaller grain size than alloy A. The lower solution treating temperature allowed for alloys B and C is the major reason for the reduction in grain size. Alloy A requires a very high solution treating temperature, 1300°C, where grain growth is very rapid. Therefore, alloys B and C have a considerable advantage over alloy A in that they are both easier to process and result in superior properties. The mechanical properties of alloys B and C do not degrade as severely as alloy A but unfortunately the additions of V and V + Ti only retard the embrittlement,not eliminate it.

Another method successfully used in retarding the embrittlement is the thermomechanical treatment applied to alloy B. Good elongations and very high tensile strengths were observed, but magnetic measurements must first be made in order to determine if the method is compatible with satisfactory magnetic properties.

The magnetic properties and the mechanical properties are both affected by spinodal decomposition. It has been shown that the mechanical hardening, i.e. yield stress, is analogous to the magnetic hardening, i.e. coercive force (H_c). The method of step aging is the most effective method of improving both the mechanical hardness and the coercive force (H_c), i.e. both properties improve with reduced aging temperature.

Hardening due to spinodal decomposition appears to be quite similar to that found for the aged Fe-Cr binary alloys. The addition of Co shifts the miscibility gap to higher temperatures, resulting in a more rapid hardening than has been found for the Fe-Cr alloys. Hardening has been explained by a combination of an athermal and a thermal contribution. The athermal or temperature independent part

accounts for the ability to pin dislocations at the $\alpha_1 - \alpha_2$ interface. And the thermal or temperature dependent part accounts for the resistance to dislocations passing through the α_2 phase.

ACKNOWLEDGEMENTS

The author is grateful to Professor Gareth Thomas for his support, encouragement, and patience throughout this study. He would like to thank Professor J. W. Morris, Jr. and Professor Iain Finnie for their review of this manuscript.

The assistance of the support staff in the Materials and Molecular Research Division of the Lawrence Berkeley Laboratory is deeply appreciated. Special thanks is extended to all my friends and colleagues that made my stay at Berkeley so truly enjoyable.

This research was supported by the Division of Materials Sciences, Office of Basic Energy Sciences, U.S. Department of Energy under Contract Number W-7405-Eng-48.

REFERENCES

1. H. Kaneko, M. Homma K. Nakamura, AIP Conf. Proc., 5, p. 1088, (1971).
2. G. Y. Chin, J. T. Plewes, and B. C. Wonsiewicz, J. Appl. Phys., vol. 49, p. 2046, March 1978.
3. B. D. Culity, Introduction to Magnetic Materials, pub. Addison-Wesley, 1972, p. 383.
4. Y. Belli, M. Okada, G. Thomas, M. Homma, and H. Kaneko, J. Appl. Phys., vol. 49, 2049, March 1978.
5. R. W. Carpenter, ACTA Met., 1967, vol. 15, p. 1297.
6. L. H. Schwartz, S. Mahajan, and J. T. Plewes, ACTA Met., 1974, vol. 22, p. 601.
7. S. D. Dahlgren, Met. Trans. A, 1976, vol. 7A, p. 1661.
8. S. D. Dahlgren, Met. Trans. A, 1977, vol. 8A, p. 347.
9. E. P. Butler and G. Thomas, ACTA Met., 1970, vol. 18, p. 347.
10. R. J. Livak and G. Thomas, ACT Met., 1971, vol. 19, p. 497.
11. K. G. Kubarych, M. Okada, and G. Thomas, Met. Trans. A, 1978, vol. 9A, 1265.
12. R. Lagneborg, ACTA Poly. Scand., Chemistry including Metallurgy Series No. 62, (1967).
13. E. O. Hall and S. H. Algie, Met. Rev., 1966, vol. 11, p. 61.
14. M. Okada, Ph.D. Thesis, U. C. Berkeley, 1978.
15. M. Okada, M. Homma, H. Kaneko, and G. Thomas, "34th Ann. Proc. Electron Microscopy Soc. Amer." Miami Beach, Florida, 1976, (ed.) G. W. Bailey, p. 606.

16. M. Okada, G. Thomas, M. Homma, and H. Kaneko, IEEE Trans. Magnetics, vol. Mag-14, No. 4, p. 245, (1978).

17. Y. Belli, M. S. Thesis, U. C. Berkeley, 1978.

18. YE. A. Vintaykin, G. G. Urushadze, J. S. Belyatskaya, and YE. A. Sukharouva, Fiz. metal. metalloved, 1974, vol. 38, p. 102.

19. W. Köster, Arch Eisenhuettenw. 6, 113 (1932).

20. S. Rideout, W. D. Mamly, E. L. Kamen, B. S. Lement, and P. A. Beck, Trans. AIME 191, 872 (1951).

21. W. Köster, and G. Hufman, Arch. Eisenhuettenw. 30, 249, (1959).

22. R. M. Fisher, E. J. Dulis, K. G. Carroll, Trans. Met. Soc. AIME, 197, 690, (1953).

23. E. Z. Vintaikin and A. A. Loshmanov, Phys. Met. Metallography, 1966, vol. 22. p. 473.

24. R. O. Williams and H. W. Paxton, J. Iron and Steel Inst., 185, 358 (1957).

25. R. O. Williams, Trans. Met. Soc. AIME, 212, 497, (1958).

26. M. J. Marcinkowski, R. M. Fisher, and A. Szirmae, Trans. Met. Soc. AIME, 230, 676, (1964).

27. Y. Imai, M. Izumiyana, and T. Masumoto, Sci. Rep. Res. Inst., Tohuku University, Ser. A, 1966, vol. 18, p. 56.

28. R. Lagneborg, ASM Trans. Quart., 60, 67, (1967).

29. E. Z. Vintaikin, V. B. Dimitriev, and V.Yu, Kolonstsov, Fiz. Metal. Metalloved., 1969, vol. 27, p. 1131.

30. D. Chandra and L. H. Schwartz, Met. Trans., 1971, vol. 2, p. 511.

31. R. Tahara, Y. Nakamura, M. Inagaki, and Y. Iwana, Phys. Stat. Sol., (a) 41, 451, 1977.

32. H. Kaneko, M. Homma, K. Nakamura, and M. Miura, IEEE Trans. Magnetics, vol. Mag-8, p. 347, Sept. 1972.

33. L. M. Magat, G.V. Ivanova, T. P. Lapina, L. V. Solina, and Ya. S. Shur, Fiz. metal. Metal. ved., 1975, vol. 40, p. 43.

34. H. Kaneko, M. Homma, T. Fukunaga, and M. Okada, IEEE Trans. Magnetics, vol. Mag-11, no. 5, Sept. 1975.

35. H. Kaneko, M. Homma, and T. Minowa, IEEE Trans. Magnetics, vol. Mag-12, p. 977, Nov. 1976.

36. H. Kaneko, M. Homma, K. Nakamura, M. Okada, and G. Thomas, IEEE Trans. Magnetics, vol. Mag-13, p. 1325, (1977).

37. H. G. Schüller and P. Schwaab, Z. Metallkundle, 1960, vol. 51, p. 81.

38. D. A. Read and E. H. Thomas, IEEE Trans. Magnetics, 1966, vol. Mag-2, No. 3, p. 415.

39. J. W. Cahn, Trans. TMS-AIME, 1968, vol. 242, p. 166.

40. J. E. Hilliard, Phase Transformations, H. I. Aaronson, ed., p. 497, 1968 ASM Seminar, ASM Metals Park, Ohio.

41. M. J. Marcinkowski and D. S. Miller, Phil. Mag., 1962, vol. 7, p. 1025.

42. M. J. Blackburn and J. Nutting, J. Iron and Steel Inst., 202, p. 610, (1964).

43. D. Coutsouradis, J. M.Drapier, E. Diderrich, and L. Habraken, Cobalt, 36, 144 (1967).

44. D. J. Abson and J. A. Whiteman, J. Iron and Steel Inst., 208, 594, (1970).

45. ASM Handbook Eighth Edition, Vol. 8, Metallography, Structures and Phase Diagrams, 1973, p. 98.

46. N. J. Petch, J. Iron and Steel Inst., vol. 173, (1935), p. 25.

47. J. T. Plewes, Met. Trans. A, 1975, vol. 6A, p. 537.

48. W. P. Longo and R. E Reed-Hill, Scripta Met., vol. 4, (1970), p. 765.

49. M. A. Meyers, Met. Trans. A., vol. 8A, (1977), p. 1582.

50. ASM Handbook, Eighth Edition, Vol. 9, Fractography and Atlas of Fractographs, pub. 1974, p. 69.

51. Grain Boundary Structures and Properties, G. A. Chadwick and D. A. Smith, eds., A. P. London, 1976.

52. R. Lagneborg,ACTA Met., vol. 15, 1967, p 1737.

53. R. O. Williams, ACTA Met., vol. 5, 1957, p. 385.

54. D. J. Maykuth and R. J. Jaffee, Ductile Chromium, p. 229, The American Society for Metals, 1957.

55. J. R. Stephens and W. D. Klopp, Trans. Met. Soc. AIME, 242, 1837, (1968).

56. M. J. Marcinkowski, Journal of Metals, vol. 93, 476, (1964-65).

57. R. Gronsky, Ph.D. Thesis, U. C. Berkeley, 1976.

FIGURE CAPTIONS

Fig. 1. Demagnetized curves of various commercial magnets in comparison with the Fe-Cr-Co alloys (Ref. 14).

Fig. 2. Isothermal sections of the Iron-Chromium-Cobalt ternary system according to Köster (19) and Rideout, et al. (Ref. 20).

Fig. 3. Vertical section of the Fe-Cr-Co phase diagram at 15 wt% Co. Diagram represents phases present after the 1 hr holding time (Ref. 35).

Fig. 4. Vertical section of the Fe-Cr-Co phase diagram at 15 wt% Co and 5 wt% V. Diagram represents phases present after 1 hr holding time (Ref. 35).

Fig. 5. Vertical section of the Fe-Cr-Co phase diagram at 15 wt% Co, 3 wt% V, and 2 wt% Ti. Diagram reprsents phases present after 1 hr holding time (Ref. 35).

Fig. 6. (a) Miscibility gap of an α phase in the Fe-Cr-Co system (Ref. 36). (b) Vertical sections of the miscibility gap along the conjugate line A, B, C, and D shown in Fig. 6a (Ref. 14).

Fig. 7. Schematic diagram of the step aging method. However, the thermomagnetic treatment was not used (Ref. 17).

Fig. 8. Schematic diagram of the step aging method used on alloy D.

Fig. 9. Sketch of the round tensile specimen.

Fig. 10. Sketch of the Charpy V-notch specimen.

Fig. 11. TEM micrograph of alloy B quenched from 1000°C to ice water.

Fig. 12. TEM micrographs of the isothermally aged alloy A at 600°C for 1 hr (a), 10 hrs (b), and 100 hrs (c), and at 640°C for 1 hr (d), 10 hr (e), and 100 hrs (f).

Fig. 13. TEM micrographs of the isothermally aged alloy B at 600°C for 1 hr (a), 10 hrs (b), and 100 hrs (c), and at 640°C for 1 hr (d), 10 hr (e), and 100 hrs (f).

Fig. 14. Spinodal wavelength vs. isothermal aging time. Alloy A aged at either 600°C or 640°C.

Fig. 15. Spinodal wavelength vs. isothermal aging time. Alloy B aged at either 600°C or 640°C.

Fig. 16. TEM micrographs of the step aged alloy D after step 2 (640°C) (a), and step 4 (600°C) (b).

Fig. 17. Optical micrograph showing the grain structure of alloy A. (a) low magnification, (b) high magnification showing inclusions and pinned grain boundary.

Fig. 18. Optical micrograph showing the grain structure of alloy B. Two areas are pictured, showing the inclusions and pinned grain boundaries.

Fig. 19. TEM micrograph of alloy B aged at 600°C for 10 hrs. Grain boundary pinning by an inclusion is illustrated.

Fig. 20. TEM micrograph of alloy B aged at 640°C for 10 hrs. Grain boundary pinning by an inclusion is illustrated.

Fig. 21. Alloy A aged at 600°C for 1 hr, (a) is an optical micrograph showing typical grain boundaries and (b) is an SEM micrograph of such a grain boundary with three areas indicated. The lower x-ray energy spectrum corresponds to the inclusion, indicating it is very rich in Chromium.

The upper x-ray spectrum compares the composition of the matrix material (dots) with the grain boundary material (bars), indicating the grain boundary is rich in Chromium.

Fig. 22. An SEM micrograph of alloy A aged at 640°C for 1 hr and subsequently swaged 20% reduction in area. Note grain boundaries fail, but matrix material is ductile.

Fig. 23. Optical micrograph of the step aged alloy D (a) step 3 (600°C) (b) step 4 (580°C), showing the grain boundary phase.

Fig. 24. (a) Bright field (b) dark field pair of a grain boundary in alloy A aged at 640°C for 100 hrs, (c) is an SAD of the grain boundary area, indicating σ is the grain boundary phase. The [OTO] σ spot was used to form the dark field image. Due to the proximity to the transmitted beam, some contrast from the matrix material is evident in the image.

Fig. 25. Bright field (BF)-dark field (DF) pair showing σ in alloy A aged at 600°C for 1 hr.

Fig. 26. Dark field (a) bright field (b) pair showing σ in alloy A aged at 600°C for 5 hrs.

Fig. 27. Sigma at the grain boundary in alloy A aged at 640°C for 10 hrs.

Fig. 28. TEM micrographs showing the morphology of the σ in alloy B aged at 600°C for 1 hr. (a) bright field (b) dark field and at 600°C for 100 hrs (c) bright field (d) dark field.

Fig. 29. TEM micrograph of a triple grain junction. Differing amounts of σ are present depending upon misorientation. Alloy B aged at 600°C for 100 hrs.

Fig. 30. TEM micrograph of a triple grain junction. Alloy B aged at 640°C for 1 hr. No σ is present.

Fig. 31. TEM micrograph of a triple grain junction. Alloy B aged at 640°C for 10 hrs. Amount of σ present changes with degree of misorientation.

Fig. 32. Yield stress or fracture stress and elongation of the isothermally aged alloy A vs. aging time. The circles and squares indicate aging at 600°C and 640°C respectively. Total elongation is shown with open symbols, uniform elongation is shown with closed symbols, and the partially closed symbols refer to the total and uniform elongations being equal, i.e. no necking.

Fig. 33. Vickers microhardness of the isothermally aged alloy A vs. aging time.

Fig. 34. Charpy impact toughness of the isothermally aged alloy A vs aging time tested at room temperature.

Fig. 35. Yield stress or fracture stress and elongation of the isothermally aged alloy B vs aging time. The circles and squares indicate aging at 600°C and 640°C respectively. Total elongation is shown with open symbols, uniform elongation is shown with closed symbols, and the partially closed symbols refer to the total and uniform elongations being equal, i.e. no necking.

Fig. 36. Vickers microhardness of the isothermally aged alloy B vs aging time.

Fig. 37. Charpy impact toughness of the isothermally aged alloy B vs aging time.

Fig. 38. Yield stress or fracture stress and elongation of the isothermally aged alloy C vs aging time. The circles and squares indicate aging at 600°C and 640°C respectively. Total elongation is shown with open symbols, uniform elongation is shown with closed symbols, and the partially filled symbols refer to the total and uniform elongations being equal, i.e. no necking.

Fig. 39. Vickers microhardness of the isothermally aged alloy C vs aging time.

Fig. 40. Variation of Rockwell "C" hardness and Vickers microhardness of the step aged alloy A with aging step. The circles and squares refer to the microhardness and the Rockwell "C" hardness respectively. The arrows indicate the appropriate units.

Fig. 41. Variation of Rockwell "C" hardness and Vickers microhardness of the step aged alloy B with aging step. The circles and squares refer to the microhardness and the Rockwell "C" hardness respectively. The arrows indicate the appropriate units.

Fig. 42. Variation of Rockwell "C" hardness of the step aged alloy C with aging step.

Fig. 43. Yield stress or fracture stress and elongation of the step aged alloy B vs aging step. The open symbols refer to the uniform elongation, and the partially closed symbols refer to the total and uniform elongations being equal, i.e. no necking.

Fig. 44. Yield stress or fracture stress, Vickers microhardness and coercive force of the step aged alloy D vs aging step.

Fig. 45. Yield stress and total elongation of the thermomechanically treated alloy B vs aging time. Shown for comparison is the yield stress or fracture stress and elongation of the isothermally aged alloy B vs aging time. The closed symbols refer to the step aged alloy and the open symbols refer to the isothermally aged alloy.

Fig. 46. The stress-strain curves of the thermomechanically aged alloy B for the as-rolled condition (a), and isothermal aging at 600°C for 1 hr (b), and 100 hrs (c).

Fig. 47. SEM fractographs of alloy A pulled in tension, shown in the as-quenched condition, aged at 600°C for 20 min (Fig. 47a upper photo), 10 hrs and 100 hrs (Fig. 47b upper photos) and aged at 640°C for 20 min (Fig. 47a lower photo) and 10 hrs (Fig. 47b lower photo).

Fig. 48. SEM fractograph of alloy A aged at 600°C for 10 hrs and pulled in tension, showing the presence of feathered tongues.

Fig. 49. CVN fractographs of alloy A, shown in the as-quenched condition, aged at 600°C for 1 hr (Fig. 49a upper photo), 5 hrs and 10 hrs (Fig. 49b upper photos), and aged at 640°C for 1 hr (Fig. 49a lower photo), 5 hrs and 10 hrs (Fig. 49b lower photos).

Fig. 50. SEM fractographs of alloy B pulled in tension, shown in the as-quenched condition, aged at 600°C for 20 min (Fig. 50a upper photo), 10 hrs and 100 hrs (Fig. 50b upper photo), and aged at 640°C for 20 min (Fig. 50a lower photo), 10 hrs and 100 hrs (Fig. 50b lower photo).

Fig. 51. CVN fractographs of alloy B, shown in the as-quenched condition, aged at 600°C for 1 hr (Fig. 51a upper photo), 5 hrs and 10 hrs (Fig. 51b upper photos), and aged at 640°C for 1 hr (Fig. 51a lower photo), 5 hrs and 10 hrs (Fig. 51b lower photos).

Fig. 52. SEM fractograph of alloy B aged at 600°C for 10 hrs and pulled in tension, showing the presence of feathered tongues.

Fig. 53. SEM fractographs of alloy C pulled in tension shown in the as-quenched condition, aged at 600°C for 10 hrs and aged at 640°C for 10 hrs.

Fig. 54. SEM fractographs of the step aged material
Alloy D: (a) step 2 (640°C), (b) step 4 (600°C)
Alloy B: (c) step 4 (600°C), (d) step 5 (580°C).

Fig. 55. CVN fractographs of alloy B step aged. (a) step 4 (600°C), (b) step 7 (540°C).

Fig. 56. SEM fractograph of the thermomechanically treated alloy B (a) aged at 600°C for 20 min (b) aged at 600°C for 10 hrs.

Fig. 57. TEM micrograph of alloy A aged at 640°C for 100 hrs. Dislocations are seen to lie in the $\alpha_1 - \alpha_2$ interface. The areas of bright contrast are caused by a 2 difrracted beam being inside the objective aperture.

Fig. 58. The variation in solid solution hardening of Cr (solvent) with various alloying additions (solute). The Fe and Co data are from Stephens and Klopp (Ref. 55).

Fig. 59. Six Cr-rich compositions and their relationship to the miscibility gap in the Fe-Cr-Co system. Each composition

corresponds to an α_2 composition associated with a specific aging temperature.

Fig. 60. SEM micrographs in the vicinity of a Rockwell "C" indention of the alloys no. 1 (a), no. 2 (b), no. 4 (c), and alloy A (see Fig. 56).

Fig. 61. The variation in three point bend ductility as measured by the bend angle vs composition of the Cr rich phase. Cr is the solvent and $Fe_{.79}Co_{.21}$ is the solute.

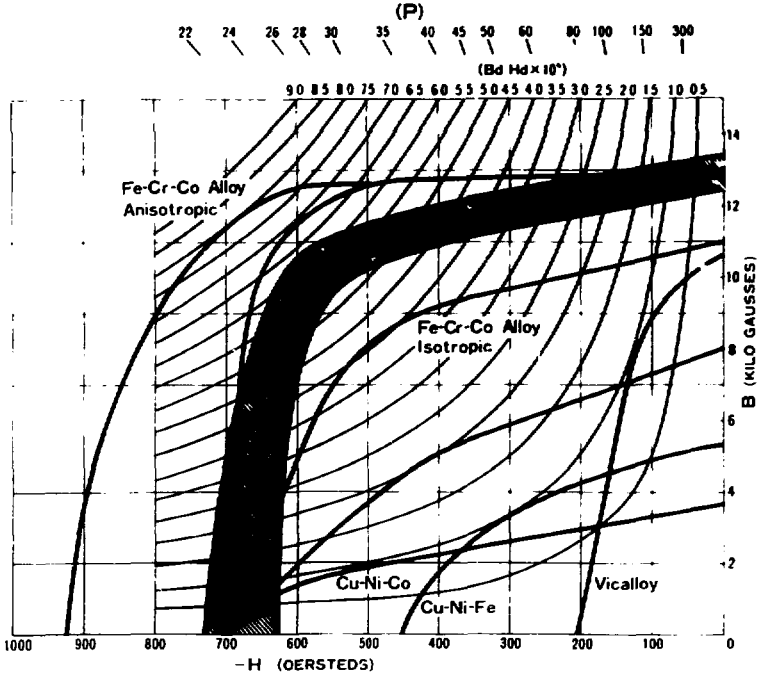

XBL 781-6968

Fig. 1

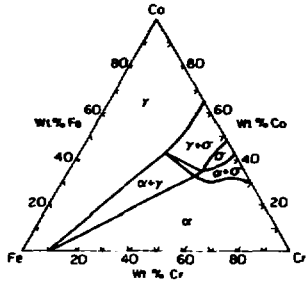

(a) 1200°C

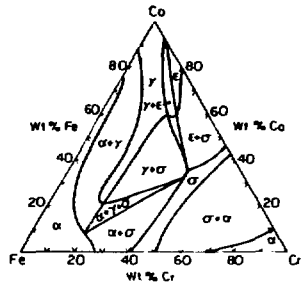

(b) 700°C

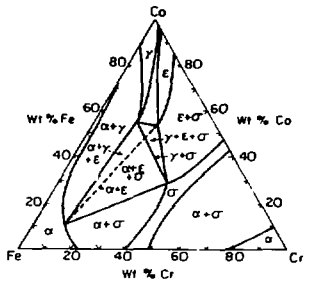

(c) 600°C

XBL 782-4566

Fig. 2

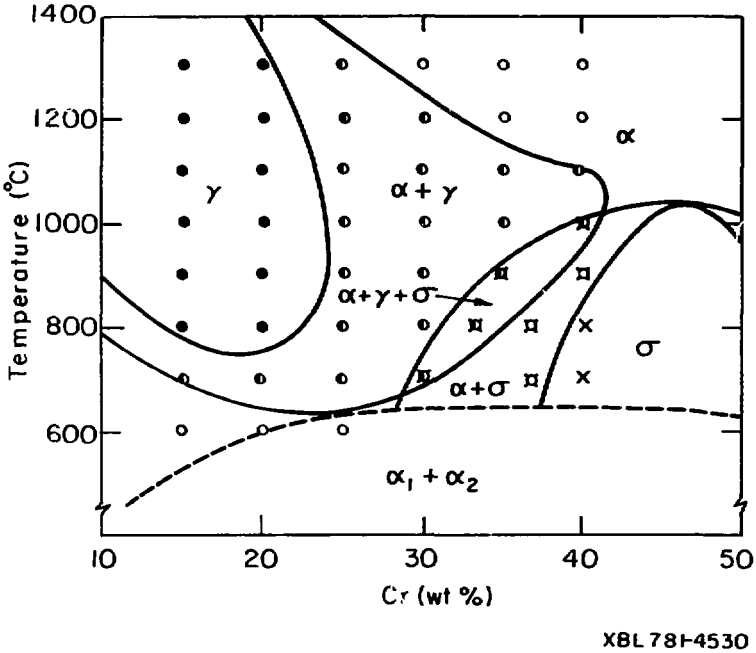
1400
1200
1000
800
600
Temperature (°C)
γ
α + γ
α
α+γ+σ
σ
α+σ
α1 + α2
10
20
30
40
50
Cr (wt %)
XBL 781-4530

Fig. 3

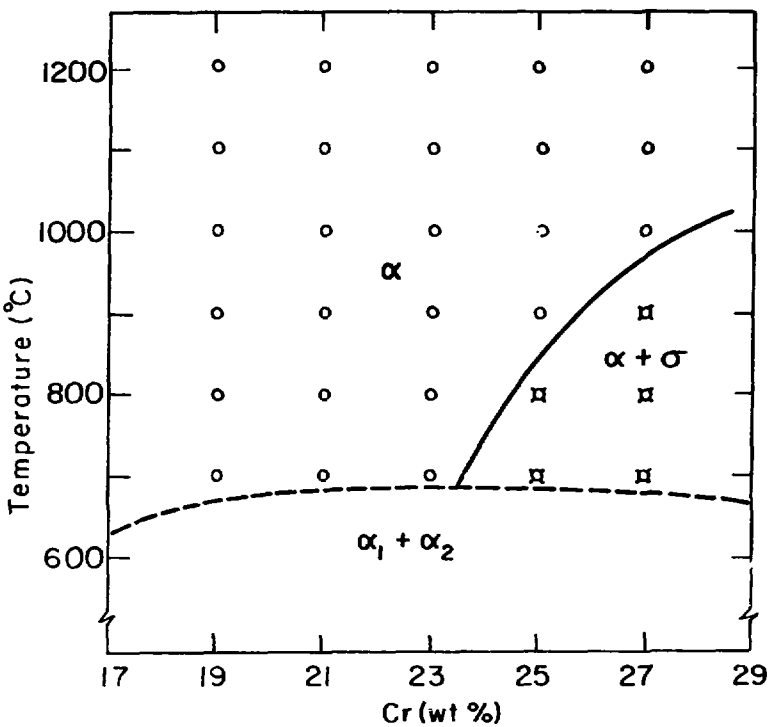
1200
1000
800
600
Temperature (°C)
α
α + σ
α1 + α2
17
19
21
23
25
27
29
Cr (wt %)
XBL 781-4532

Fig. 4

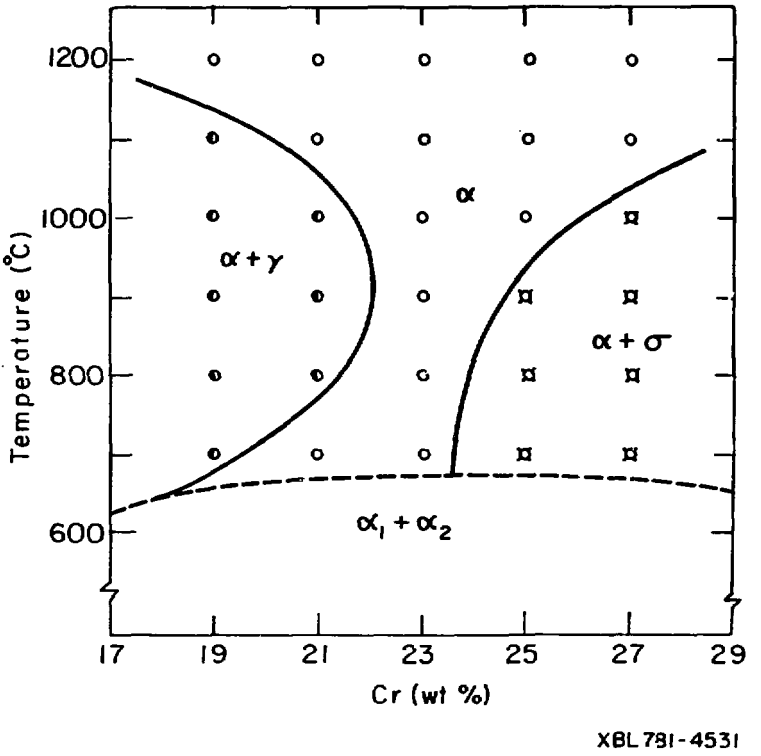
1200
1000
800
600
Temperature (°C)
α
α + γ
α + σ
α1 + α2
17
19
21
23
25
27
29
Cr (wt %)
XBL781-4531

Fig. 5

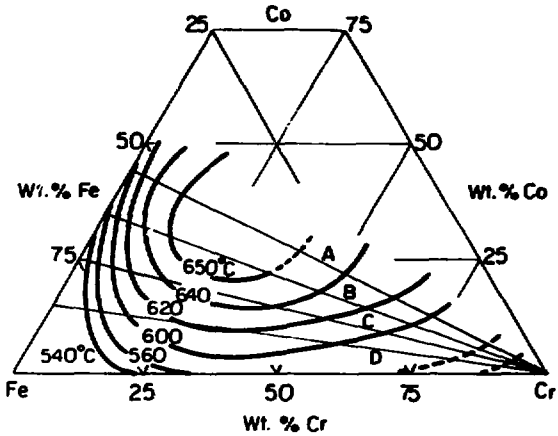

(a)

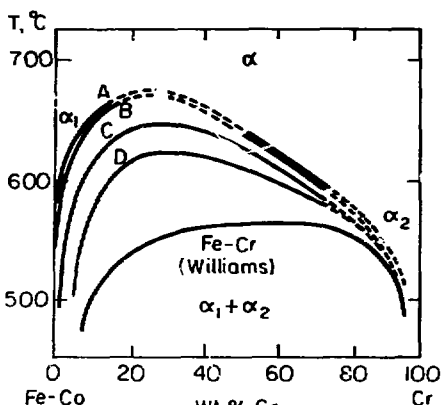

(b)

XBL782-4564

Fig. 6

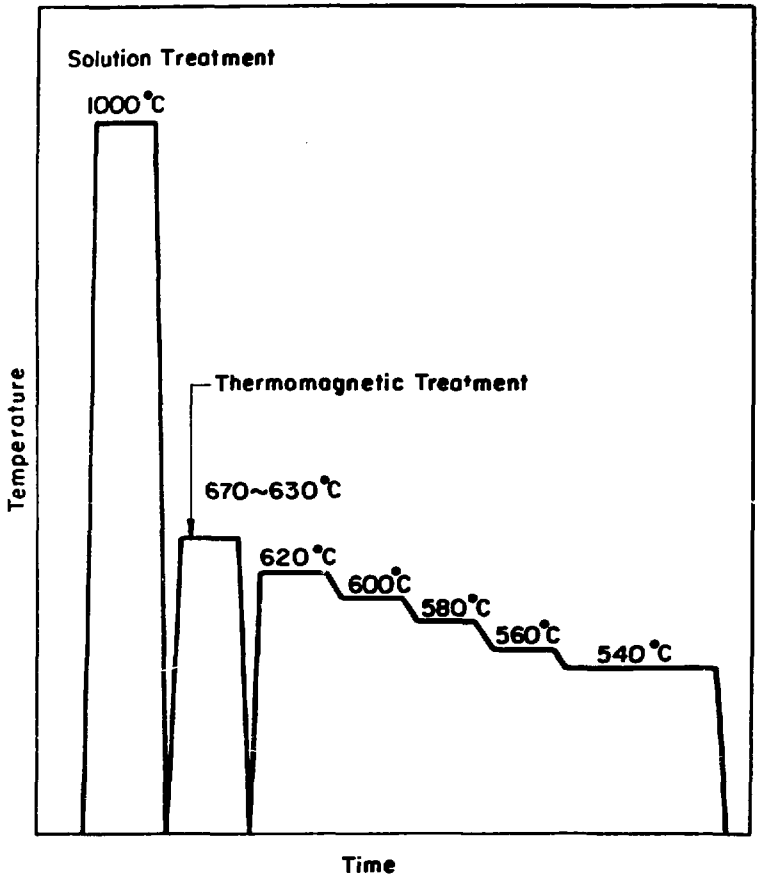
Solution Treatment
1000°C
Thermomagnetic Treatment
670~630°C
620°C
600°C
580°C
560°C
540°C
Temperature
Time
XBL 7710-6296

Fig. 7

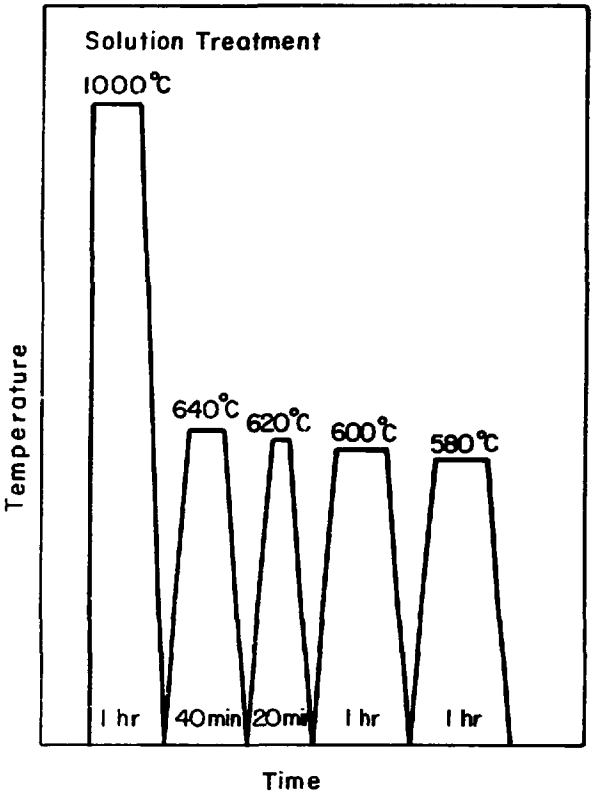
Solution Treatment
1000°C
640°C
620°C
600°C
580°C
Temperature
1 hr
40min
20min
1 hr
1 hr
Time
XBL 7910-7256

Fig. 8

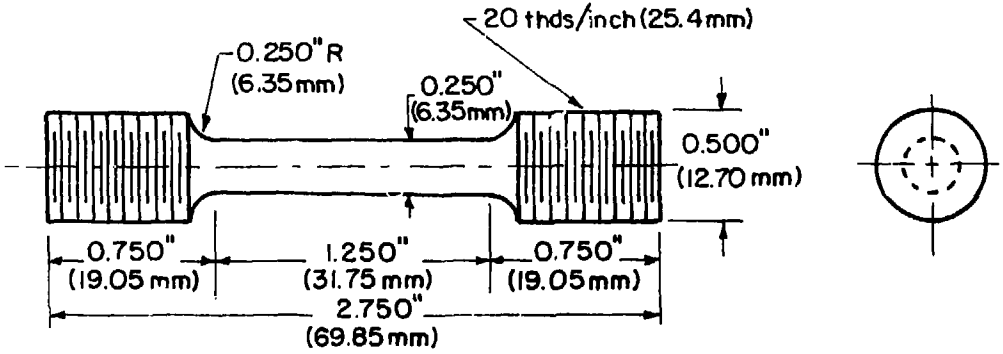

XBL 736-6280B

Fig. 9

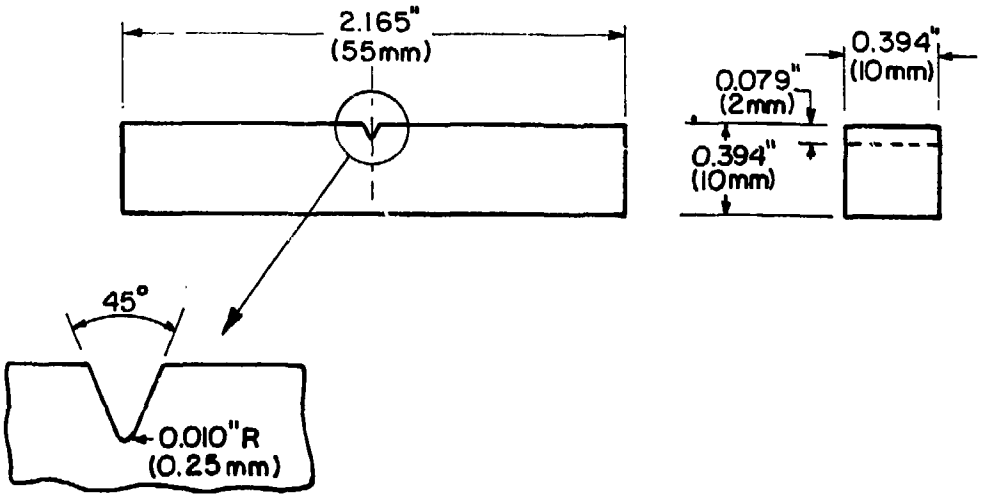

XBL 736-6280A

Fig. 10

XBB 795 6967

Fig. 11

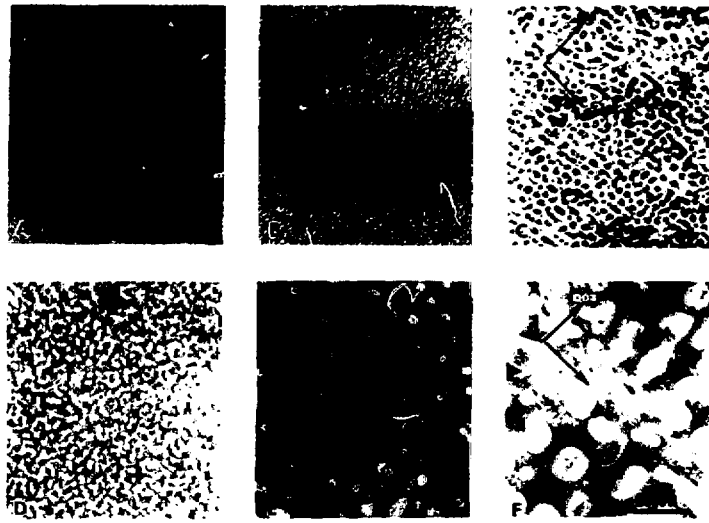

XBB 795 6969

Fig. 12

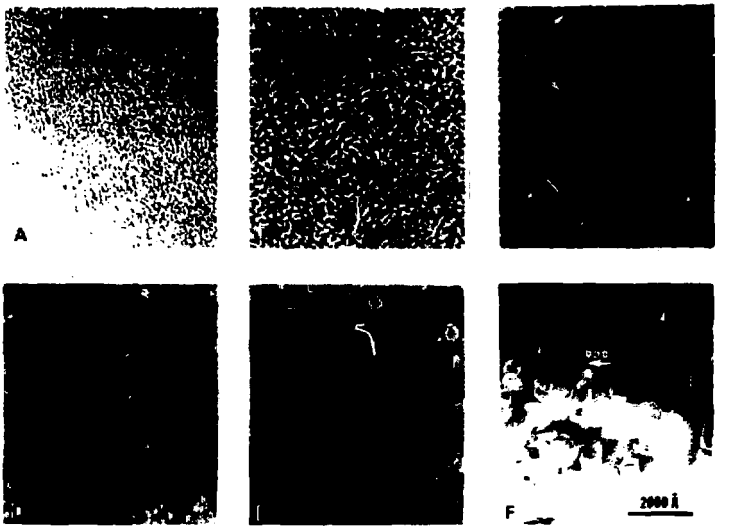

XBB 795 6970

Fig. 13

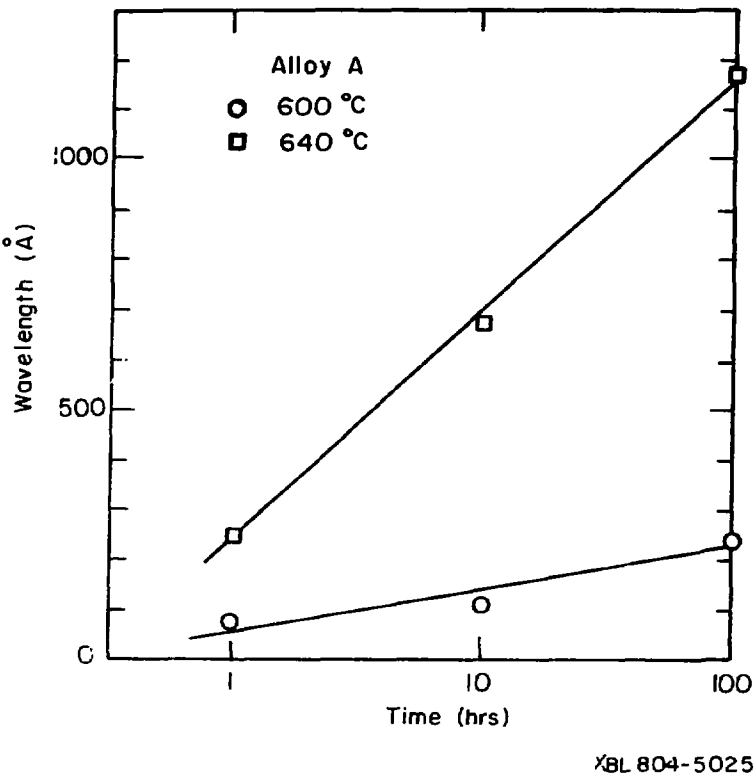
Alloy A
600 °C
640 °C
1000
500
0
Wavelength (Å)
1
10
100
Time (hrs)
XBL 804-5025

Fig. 14

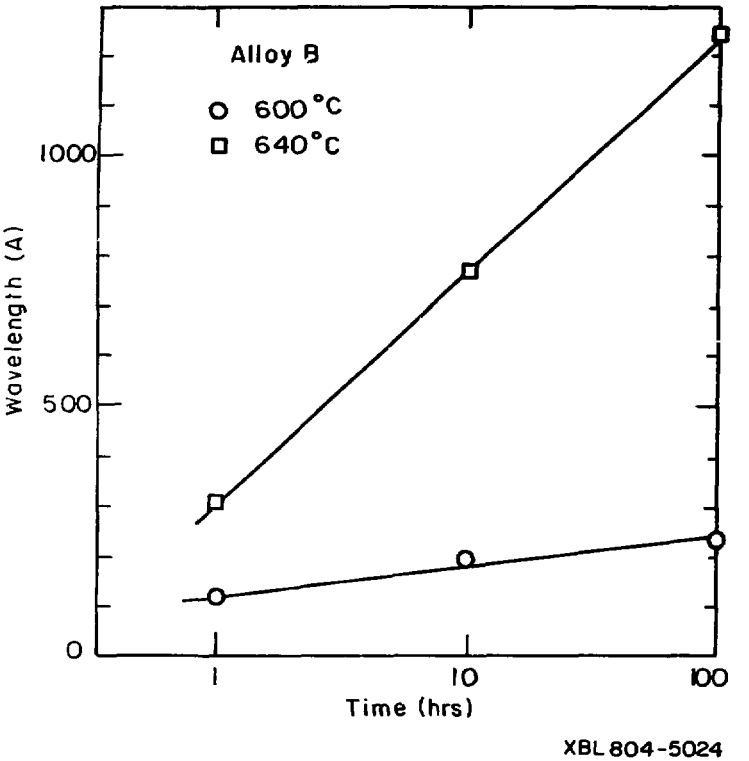
Alloy B
600°C
640°C
1000
500
0
Wavelength (Å)
1
10
100
Time (hrs)
XBL 804-5024

Fig. 15

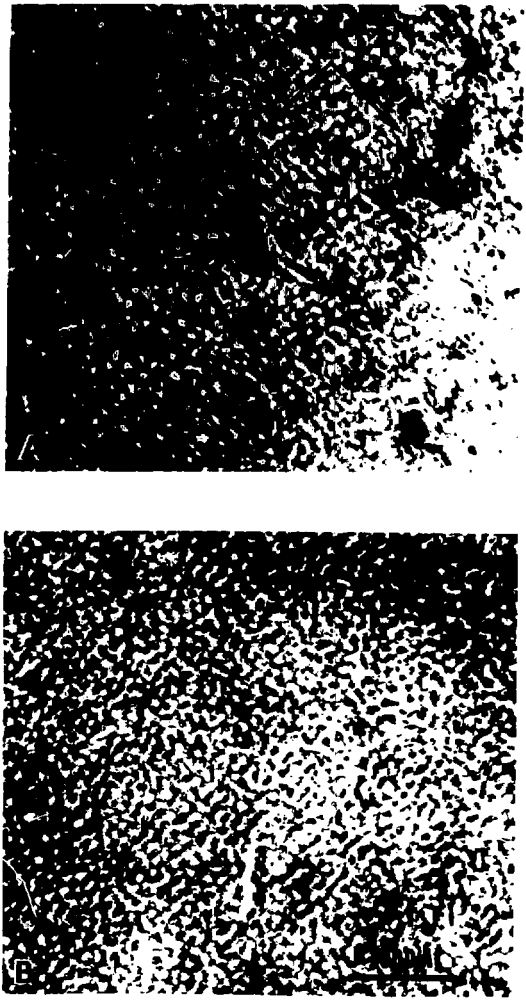

XBB 795 6966

Fig. 16

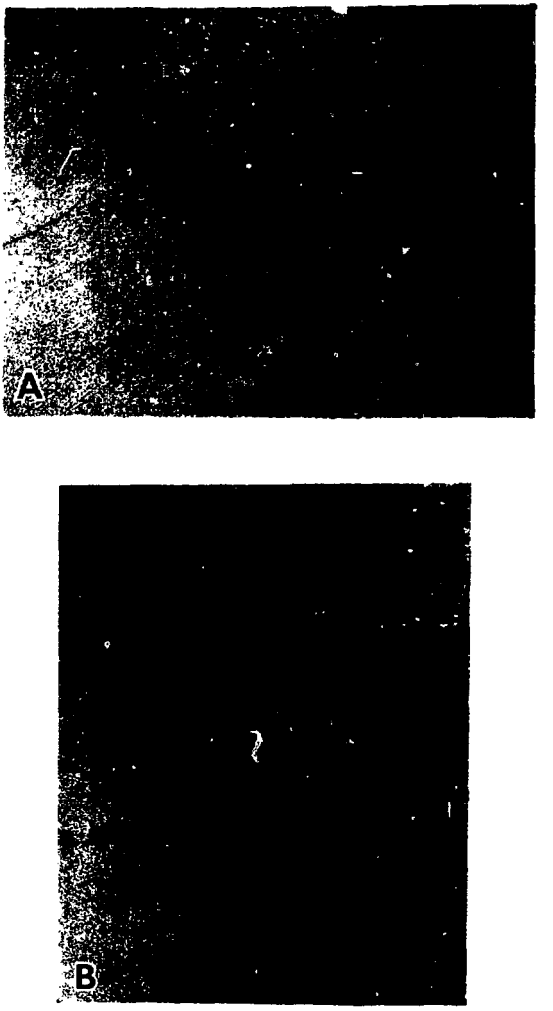

XBB 795 6624

Fig. 17

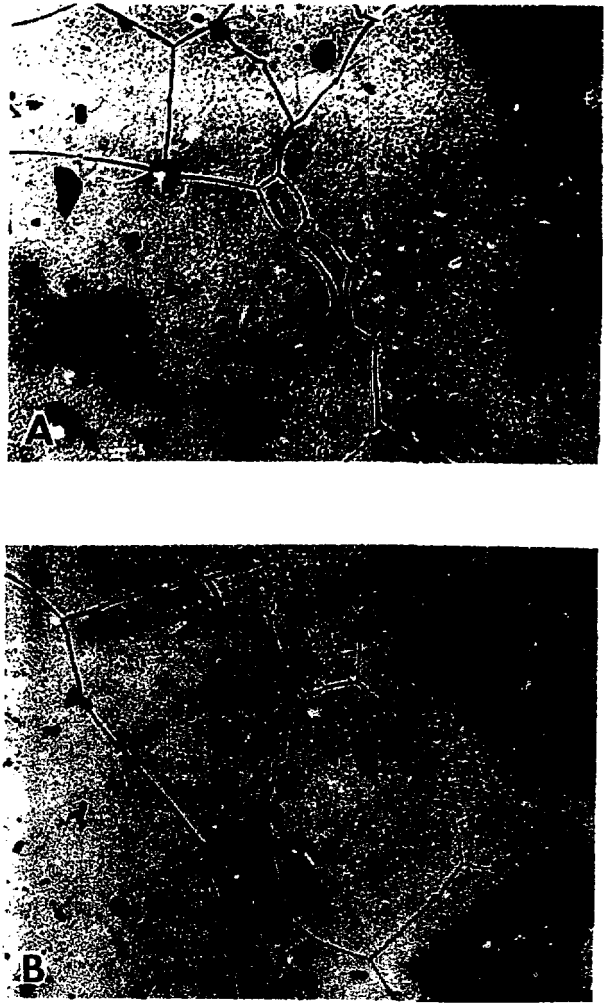

XBB 795 6622

Fig. 18

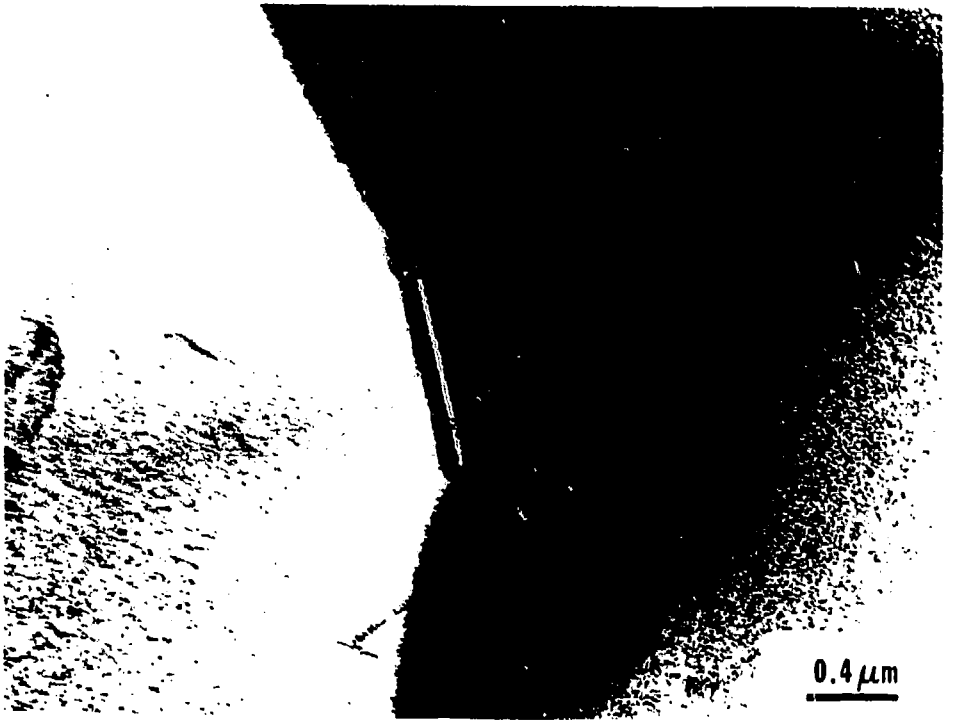

Fig. 19

XBB 795 6604

Fig. 20

XBB 795 6611

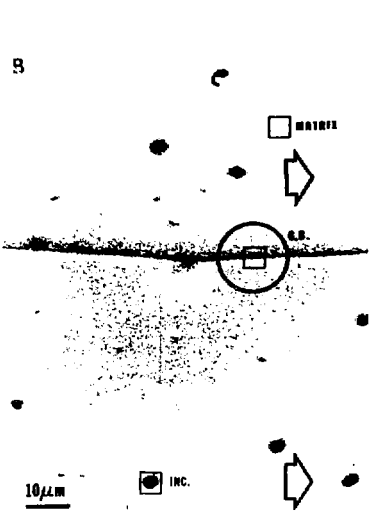

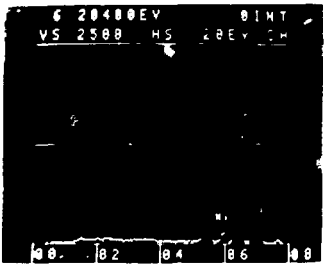

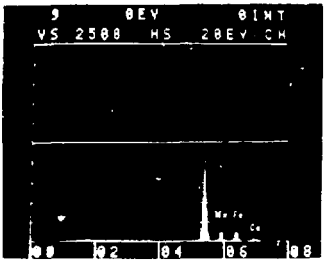

XBB 795 6625

Fig. 21

XBB 795 6609

Fig. 22

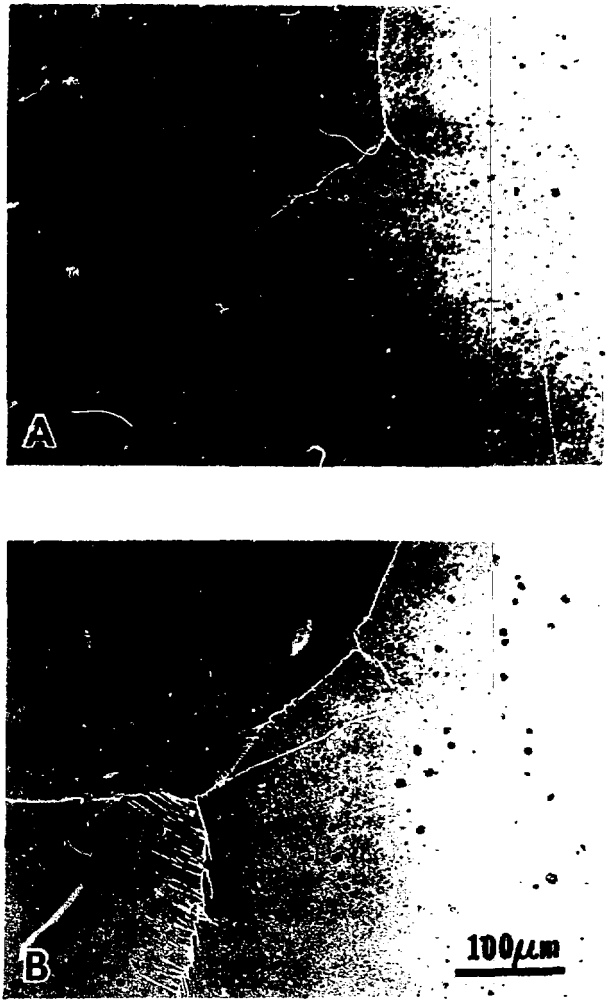

XBB 795 6623

Fig. 23

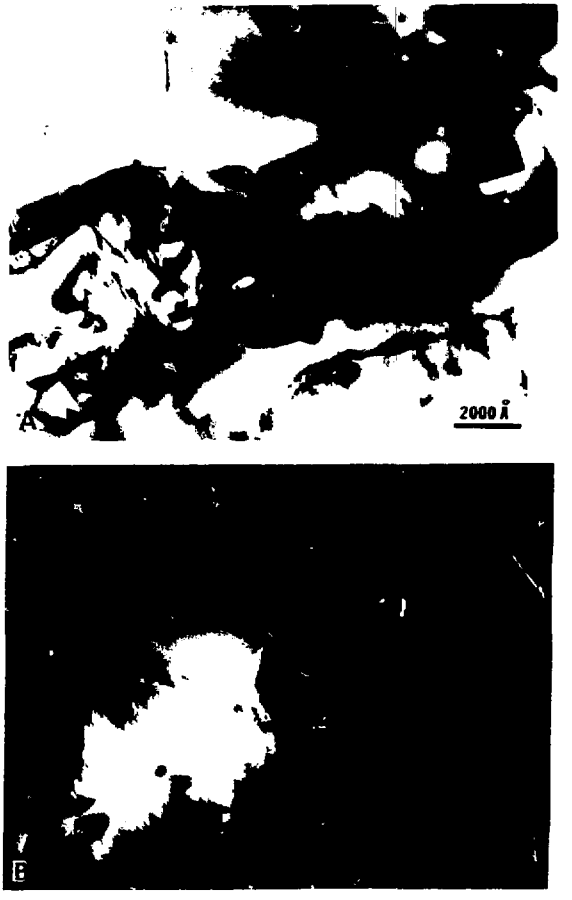

XBB 795 6964

Fig. 24A,B

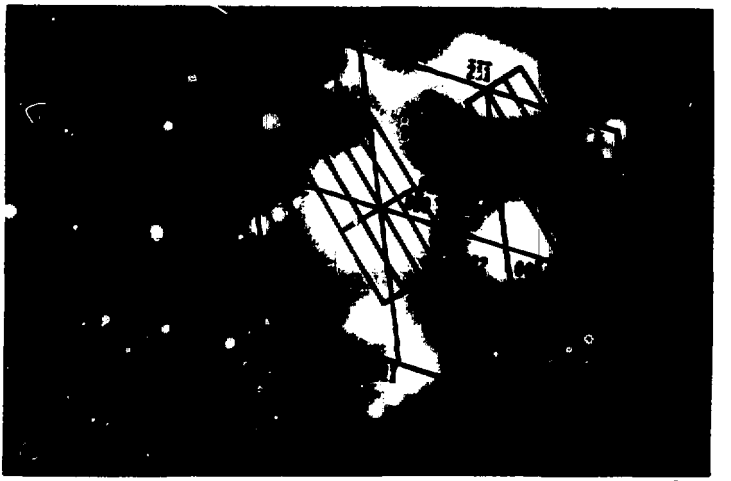

XBB 798 10566

Fig. 24C

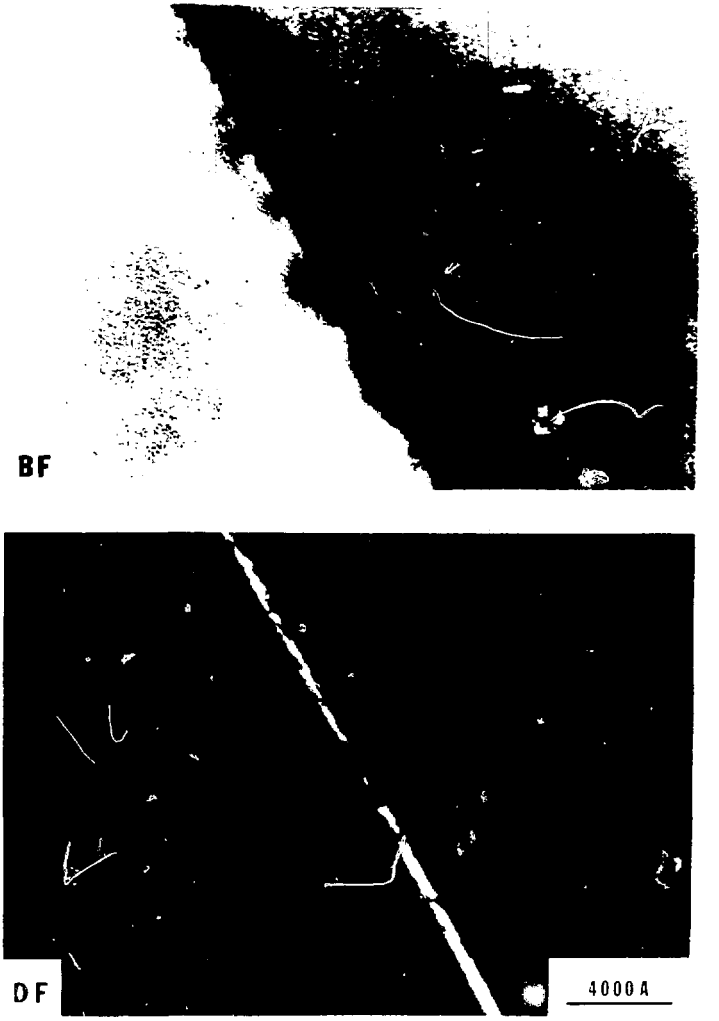

Fig. 25

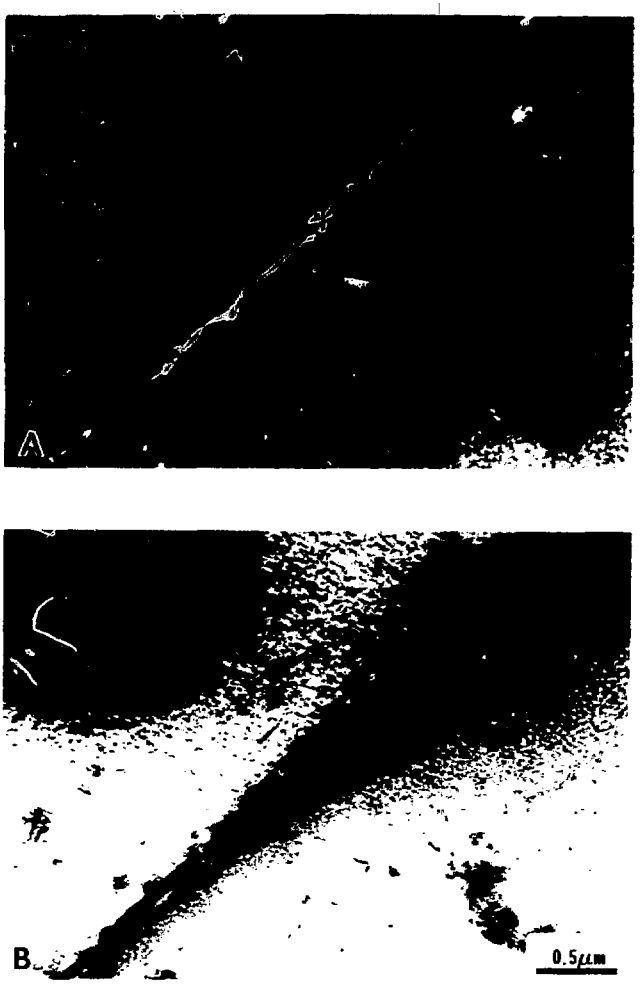

XBB 795 6607

Fig. 26

XBB 789 12457

Fig. 27

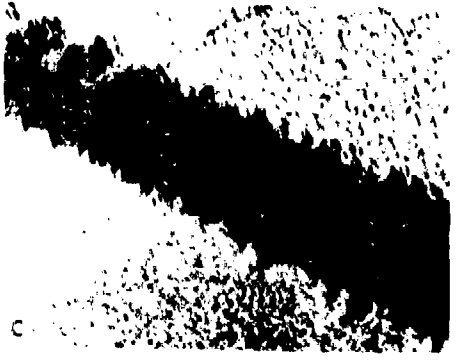

Fig. 28

XBB 795 6591

Fig. 29

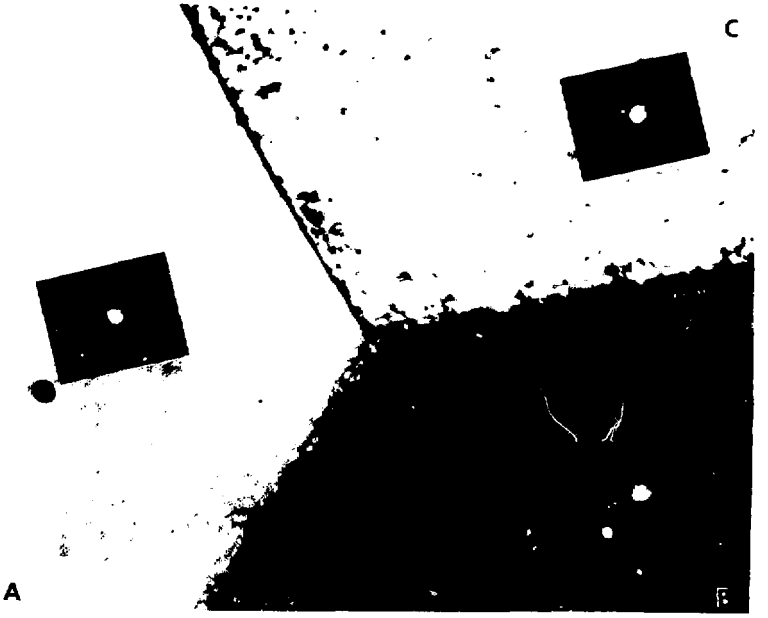

XBB 795 6973

Fig. 30

XBB 795 6971

Fig. 31

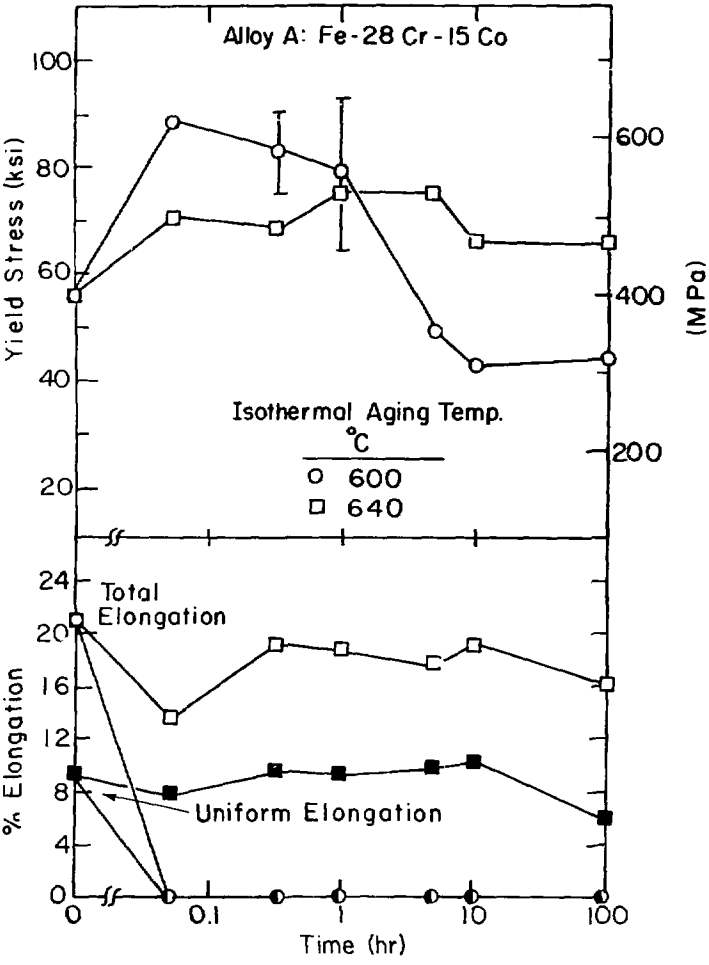
Alloy A: Fe-28 Cr-15 Co
Yield Stress (ksi)
100
80
60
40
20
600
400
200
(MPa)
Isothermal Aging Temp.
°C
o 600
□ 640
Total
Elongation
% Elongation
24
20
16
12
8
4
0
Uniform Elongation
0
0.1
1
10
100
Time (hr)
XBL 7812-6266

Fig. 32

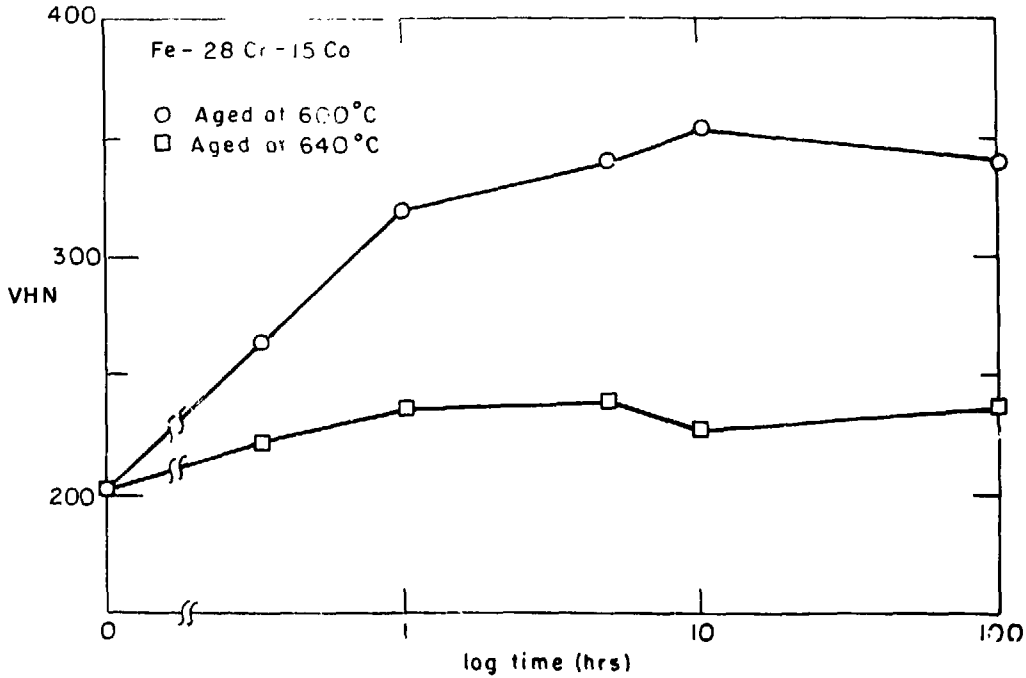
400
300
200
VHN
Fe - 28 Cr - 15 Co
O Aged at 600°C
□ Aged at 640°C
0
1
10
100
log time (hrs)
XBL 789-5820

Fig. 11

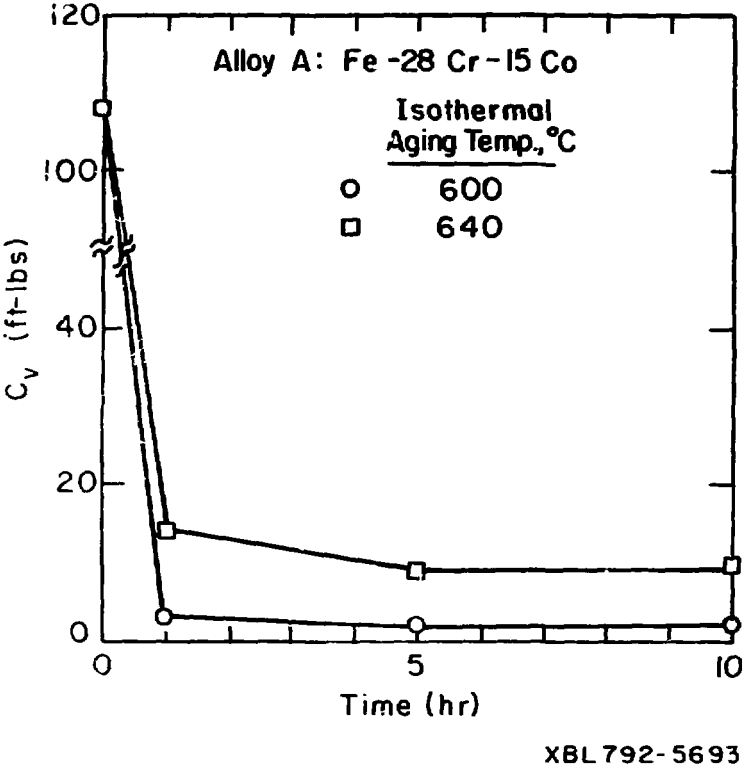
Alloy A: Fe -28 Cr - 15 Co
Isothermal
Aging Temp., °C
600
640
120
100
40
20
0
C_v (ft-lbs)
0
5
10
Time (hr)
XBL 792-5693

Fig. 14

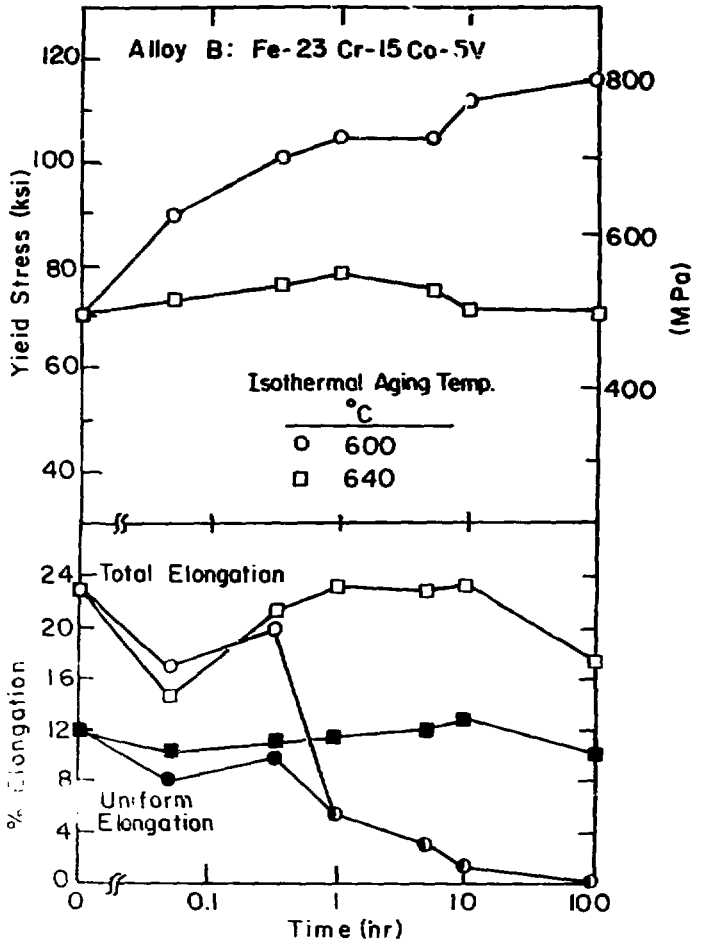
Alloy B: Fe-23 Cr-15 Co-5V
Yield Stress (ksi)
(MPa)
Isothermal Aging Temp.
°C
600
640
Total Elongation
Uniform Elongation
% Elongation
Time (hr)
XBL 7812-6267

Fig. 35

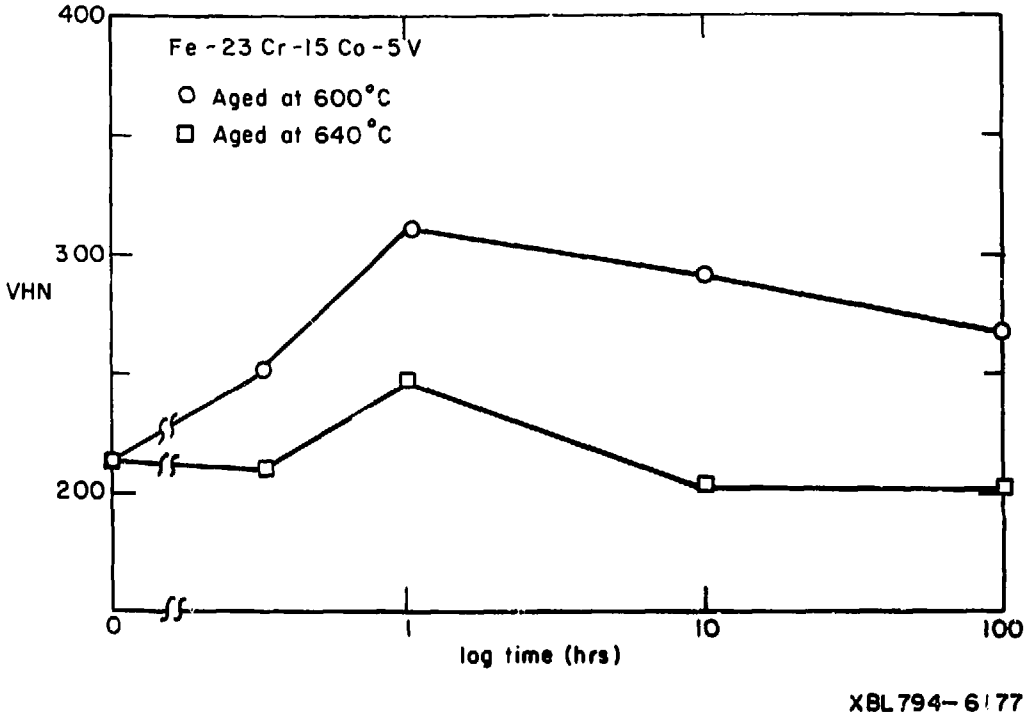
400
300
200
VHN
Fe - 23 Cr - 15 Co - 5 V
O Aged at 600°C
□ Aged at 640°C
0
1
10
100
log time (hrs)
XBL794-6177

Fig. 16

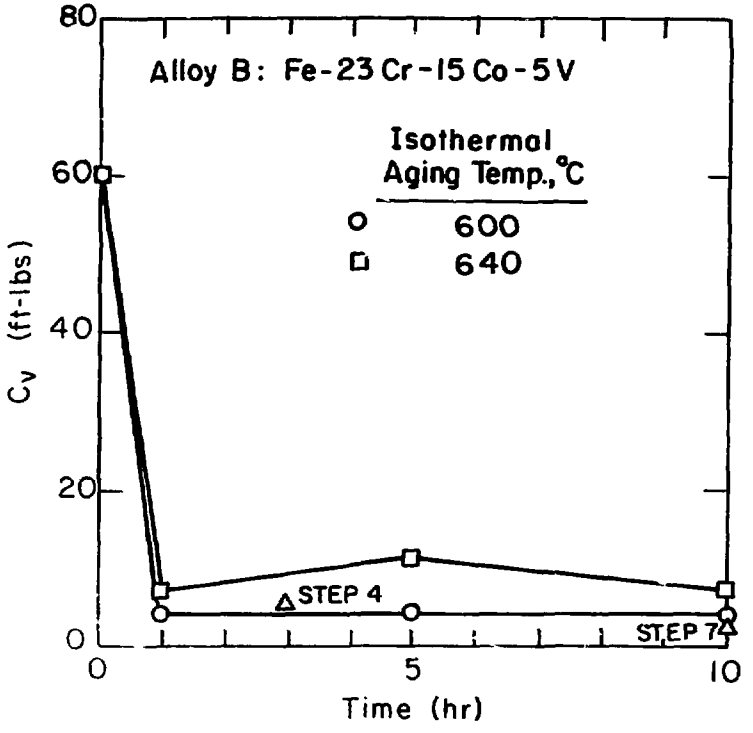
Alloy B: Fe-23 Cr-15 Co-5 V
Isothermal
Aging Temp., °C
600
640
STEP 4
STEP 7
C_v (ft-lbs)
Time (hr)
0
20
40
60
80
0
5
10
XBL792-5692

Fig. 37

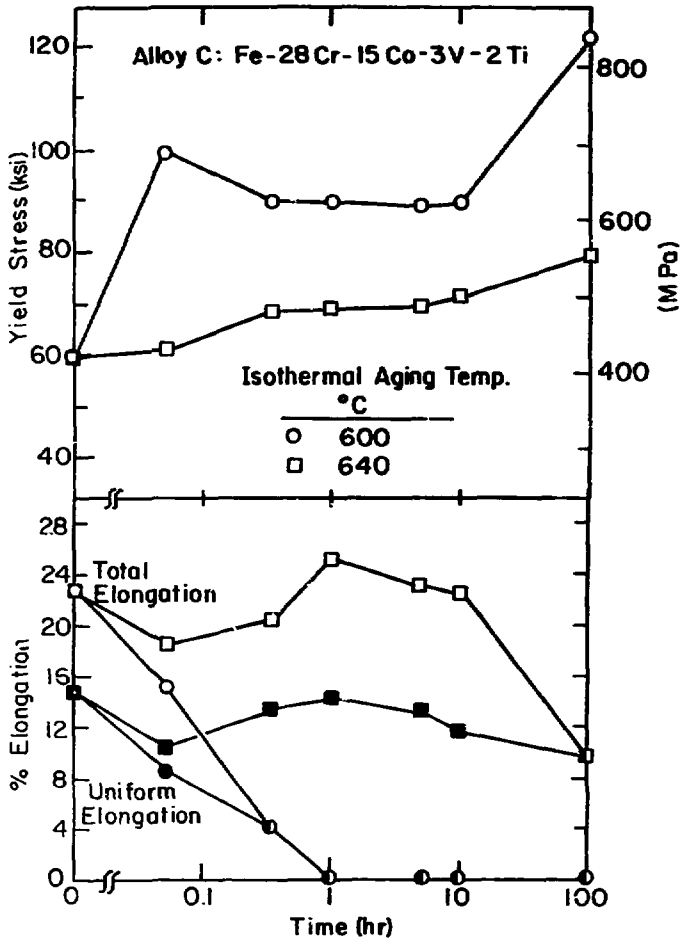
Alloy C: Fe-28Cr-15Co-3V-2Ti
Yield Stress (ksi)
(MPa)
120
100
80
60
40
800
600
400
Isothermal Aging Temp.
°C
600
640
28
24
20
16
12
8
4
0
Total Elongation
Uniform Elongation
% Elongation
0
0.1
1
10
100
Time (hr)
XBL 7812-6269

Fig. 38

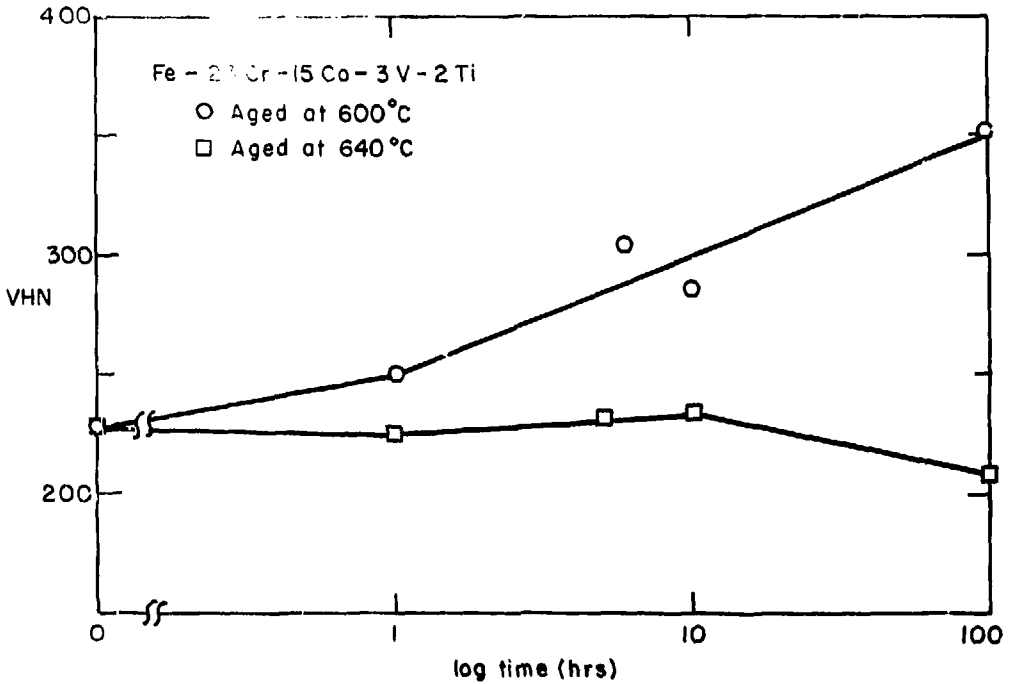

XBL 798-6718

Fig. 19

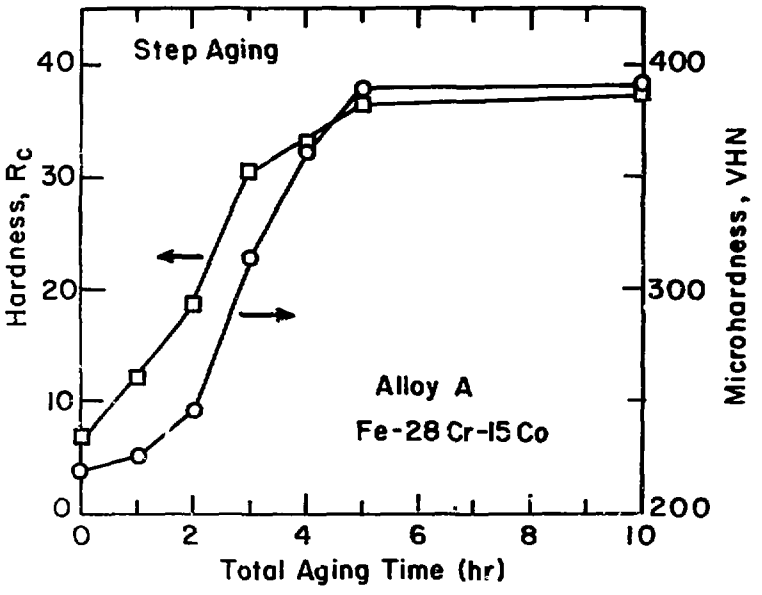
Step Aging
Alloy A
Fe-28 Cr-15 Co
Hardness, Rc
Microhardness, VHN
Total Aging Time (hr)
0
10
20
30
40
200
300
400
0
2
4
6
8
10
XBL 7812-6261

Fig. 40

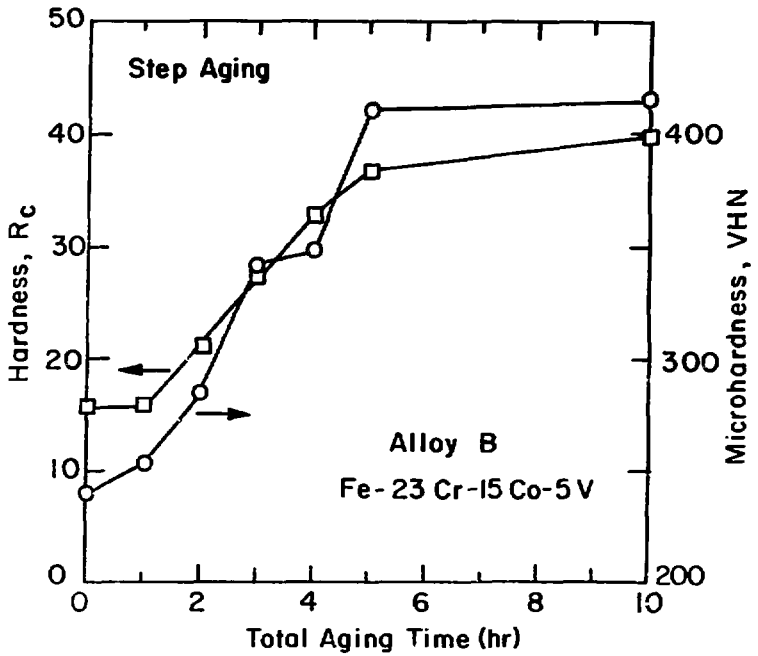

XBL 7812-6262

Fig. 41

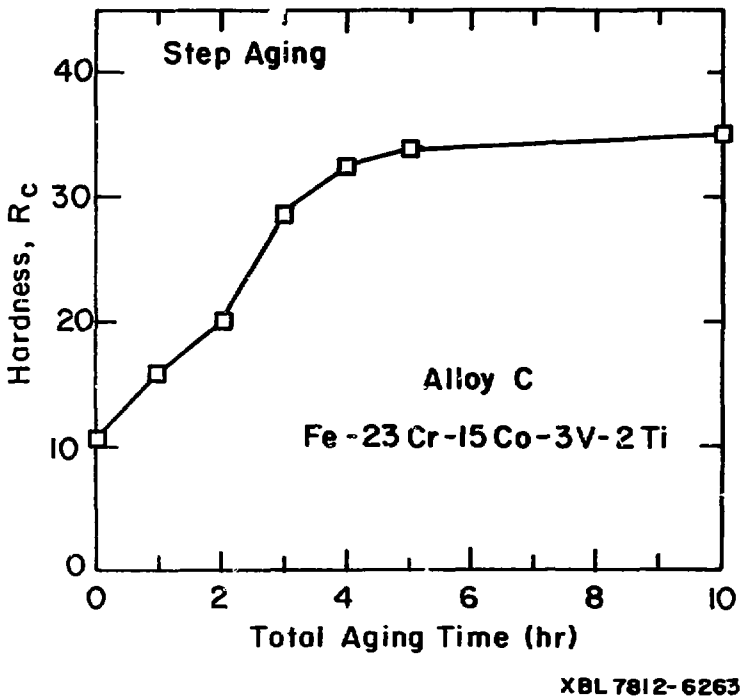
Step Aging
Alloy C
Fe-23 Cr-15 Co-3V-2 Ti
Hardness, R_c
Total Aging Time (hr)
0
10
20
30
40
0
2
4
6
8
10
XBL 7812-6263

Fig. 42

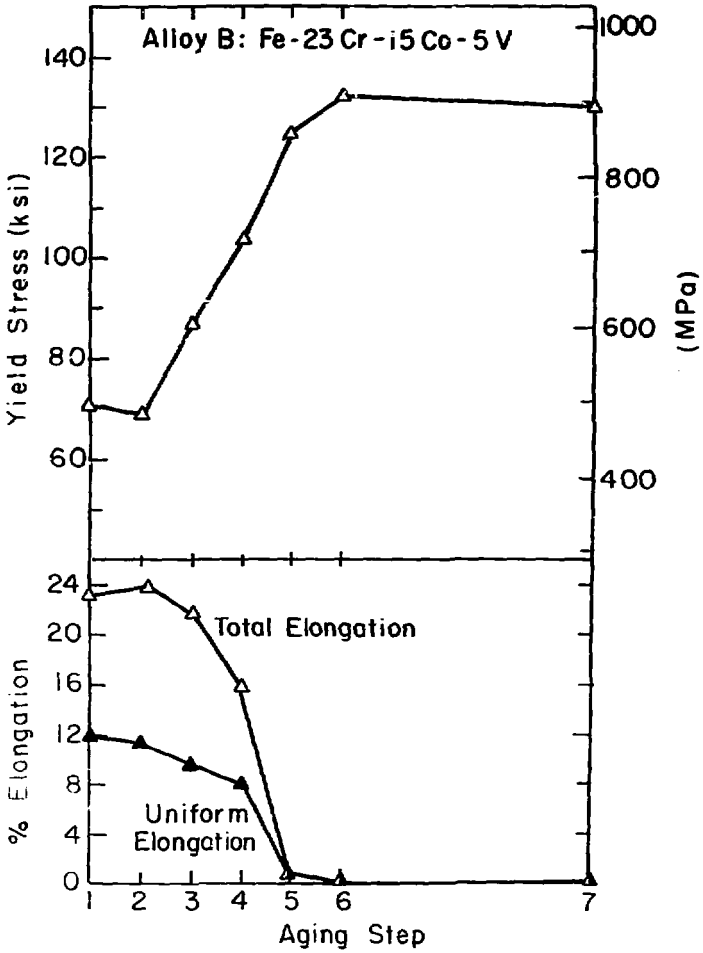

XBL 792-5691

Fig. 43

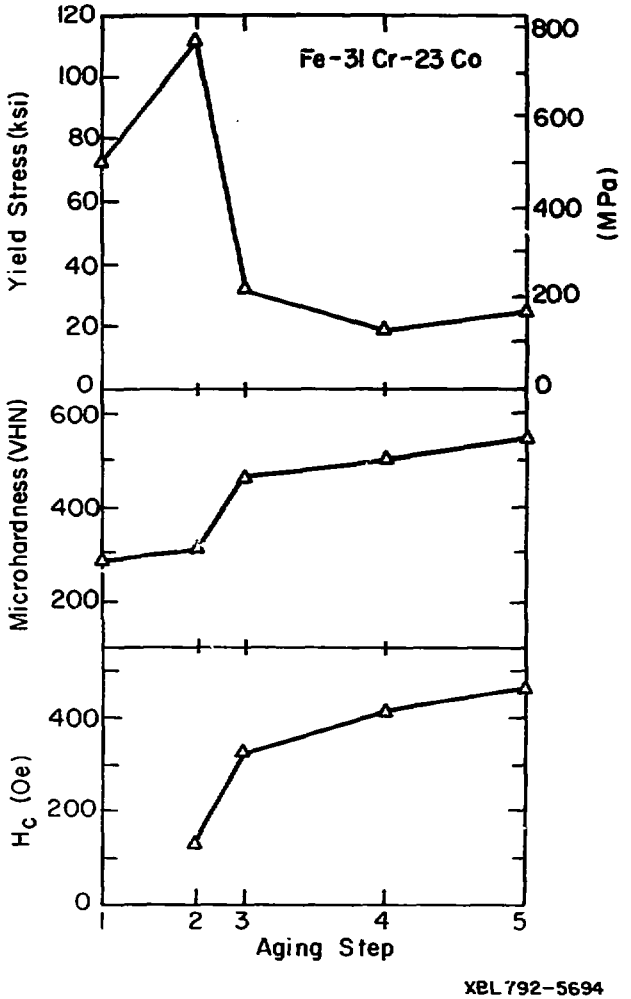
Fe-31 Cr-23 Co
Yield Stress (ksi)
(MPa)
Microhardness (VHN)
H_c (Oe)
Aging Step
XBL792-5694

Fig. 44

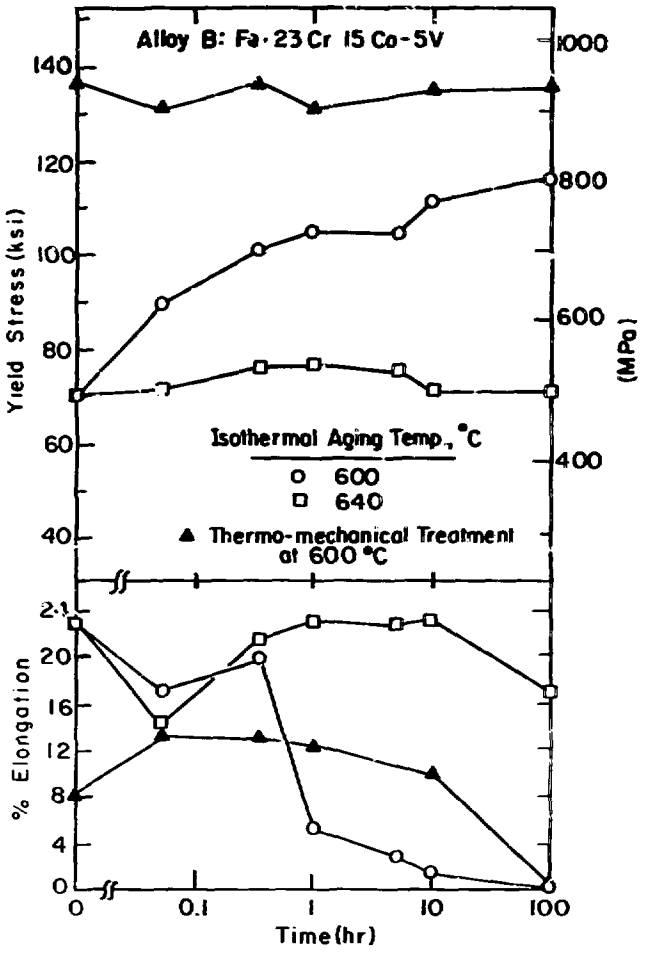
Alloy B: Fe·23Cr 15Co-5V
Yield Stress (ksi)
140
120
100
80
60
40
1000
800
600
400
(MPa)
Isothermal Aging Temp., °C
600
640
Thermo-mechanical Treatment at 600 °C
% Elongation
24
20
16
12
8
4
0
0
0.1
1
10
100
Time (hr)
XBL 78:2-6268

Fig. 45

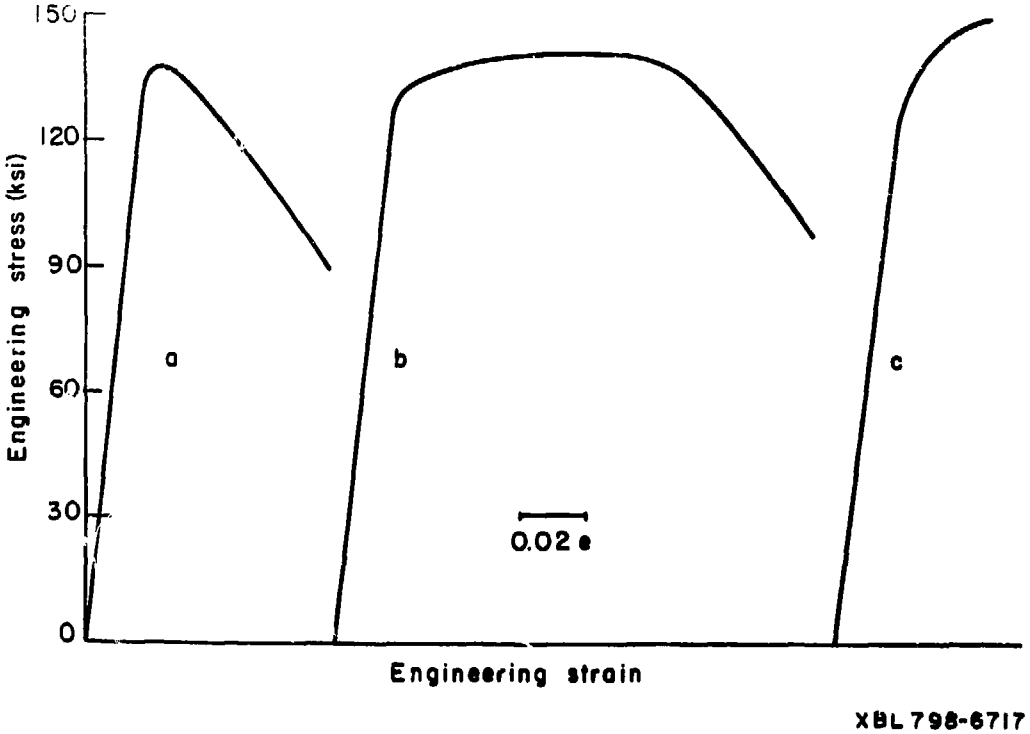
150
120
90
60
30
0
Engineering stress (ksi)
a
b
c
0.02 e
Engineering strain
XBL 798-6717

Fig. 46

XBB 795 6598

Fig. 47a

XBB 795 6599

Fig. 47b

Fig. 48

Fig. 49a

XBB 795 6595

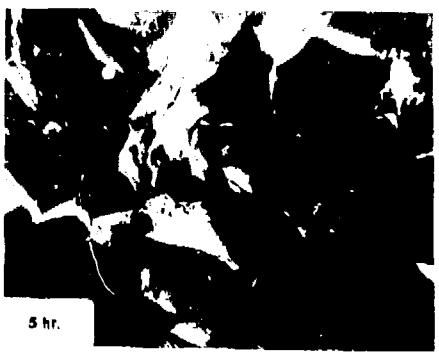

Fig. 49b

XBB 795 6596

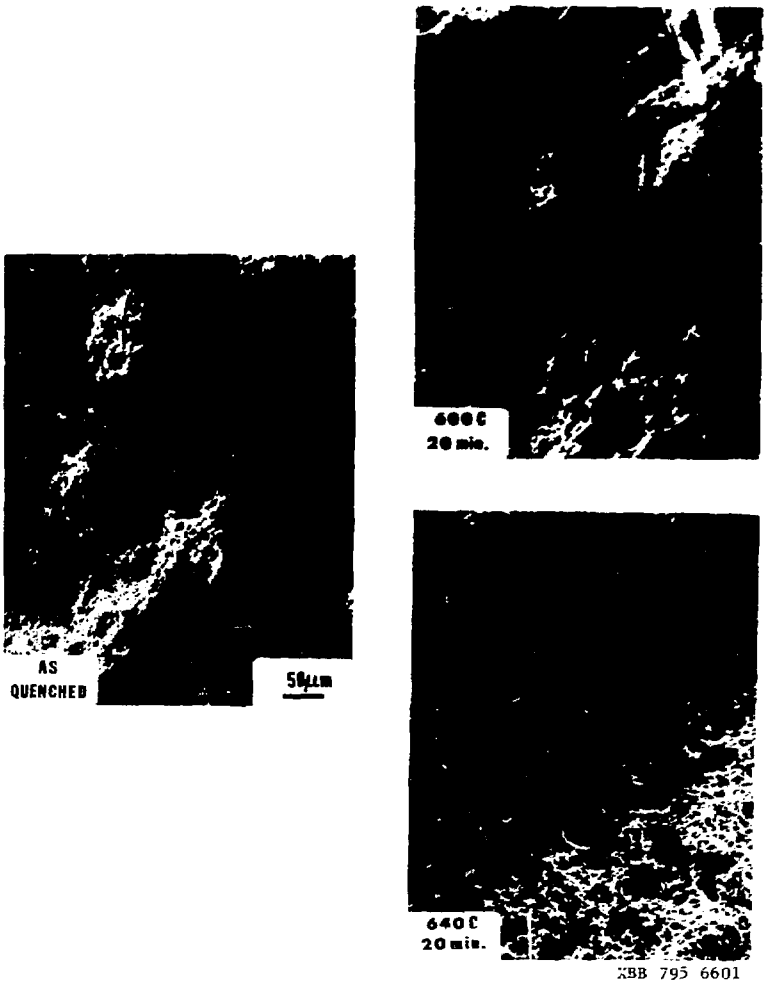

XBB 795 6601

Fig. 50a

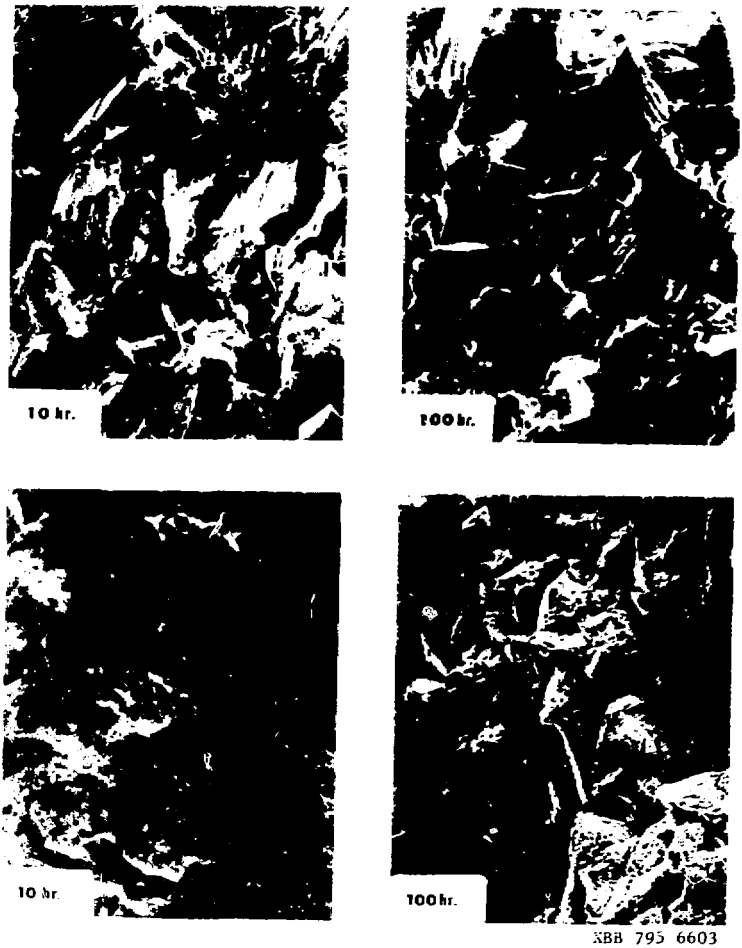

XBB 795 6603

Fig. 50b

Fig. 51a

XBB 705 6593

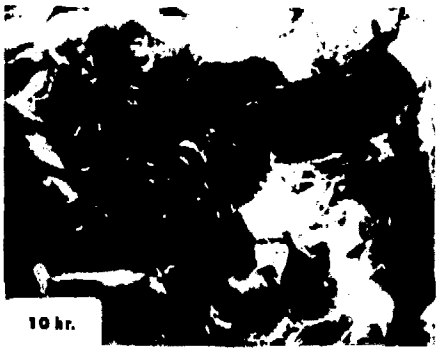

Fig. 51b

XBB 795 6594

XBB 795 10594

Fig. 52

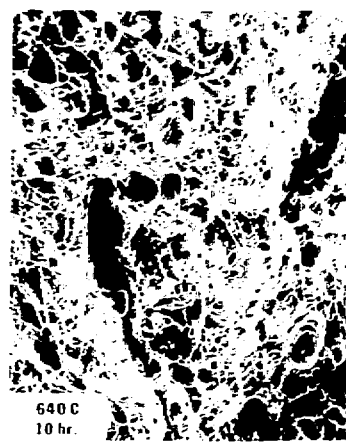

XB3 795 10568

Fig. 53

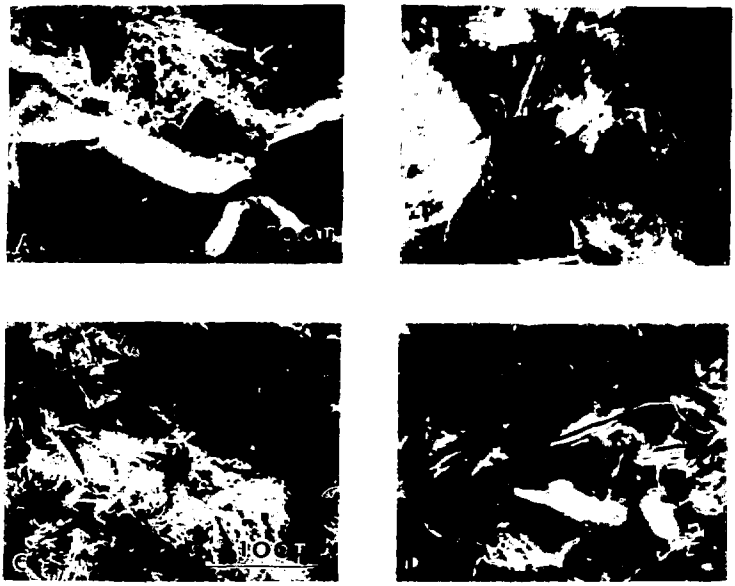

XBB 792 1669

Fig. 54

XBB 795 6608

Fig. 55

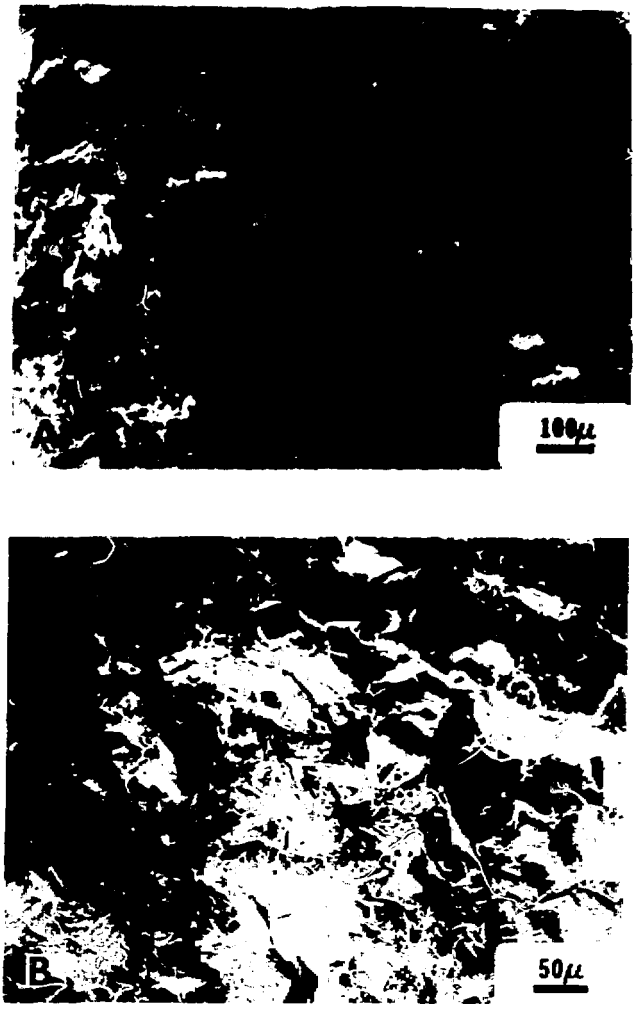

XBB 795 10567

Fig. 56

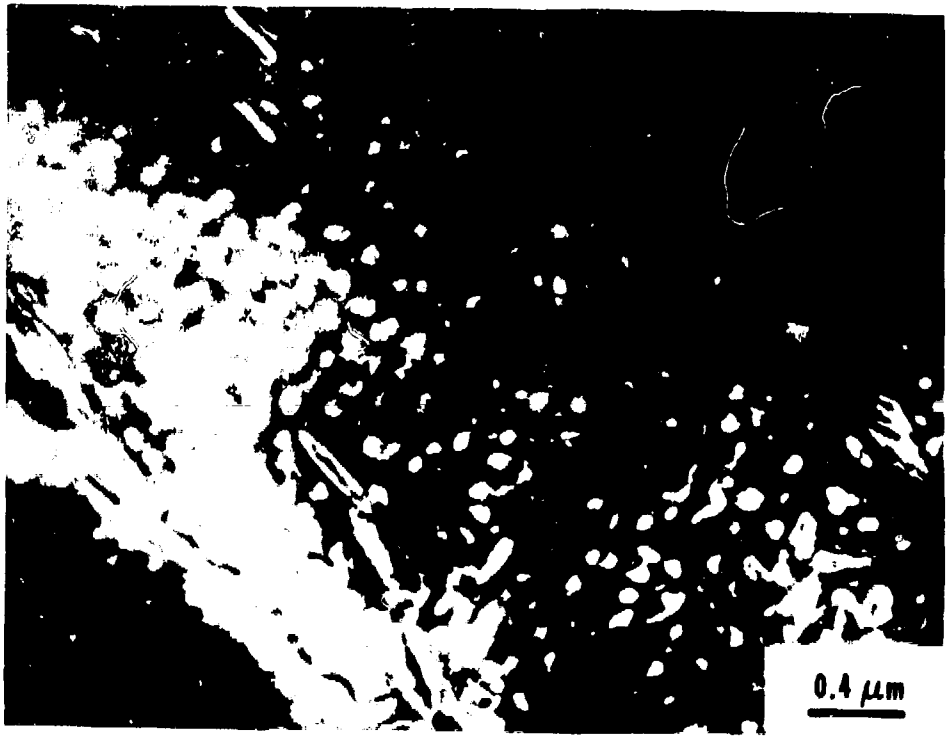

Fig. 57

XBB 795 6605

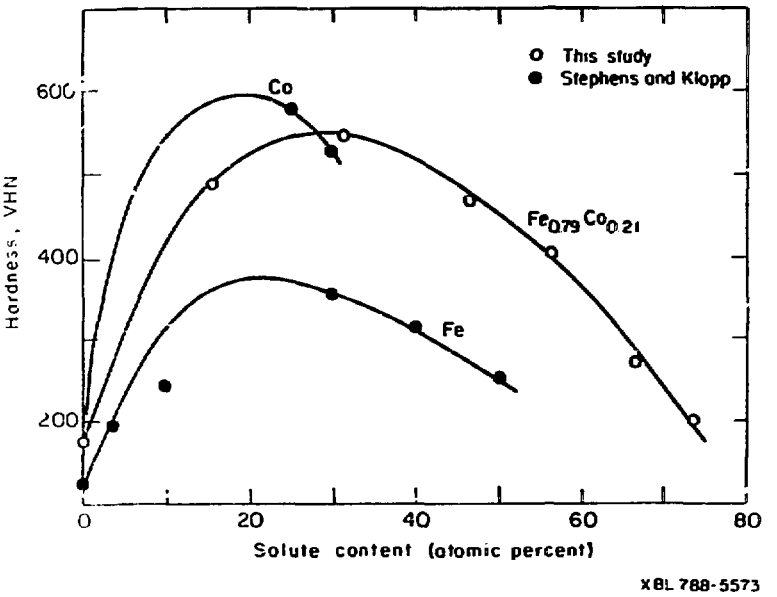
This study
Stephens and Klopp
Co
$Fe_{0.79}Co_{0.21}$
Fe
Hardness, VHN
600
400
200
0
20
40
60
80
Solute content (atomic percent)
XBL 788-5573

Fig. 58

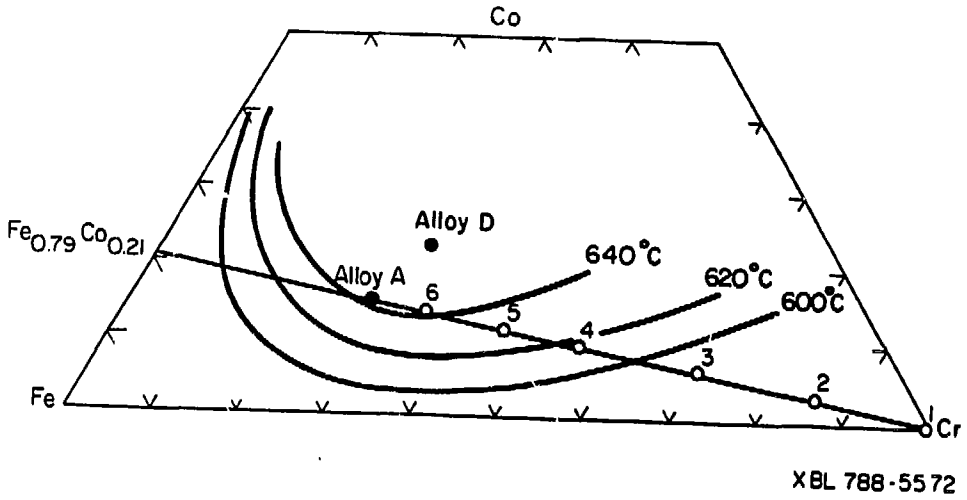
Co
Fe0.79 Co0.21
Alloy D
Alloy A
640°C
620°C
600°C
6
5
4
3
2
Fe
Cr
XBL 788-5572

Fig. 59

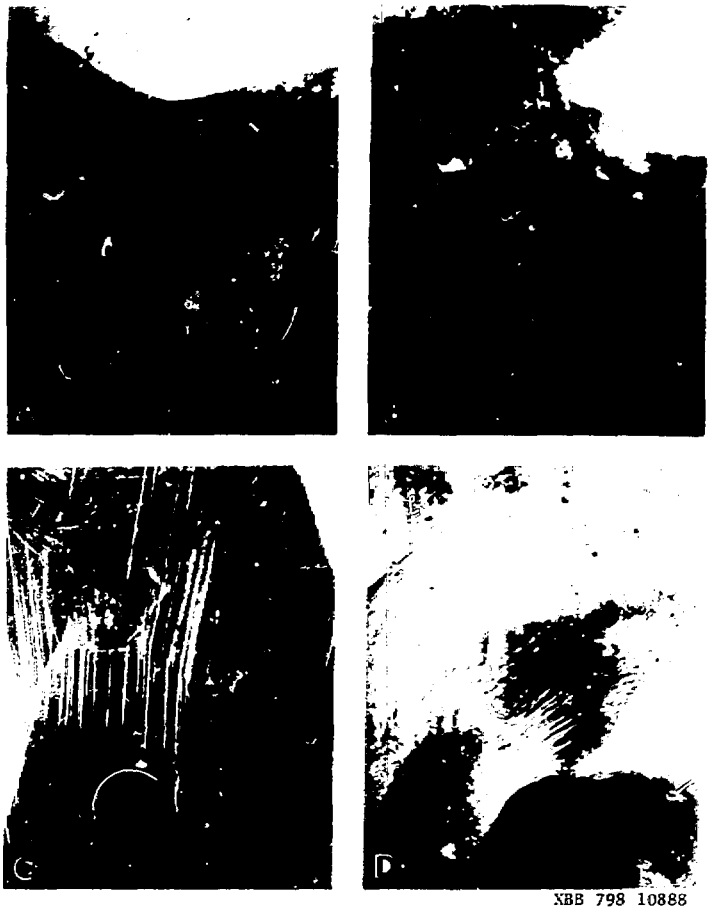

XBB 798 10888

Fig. 60

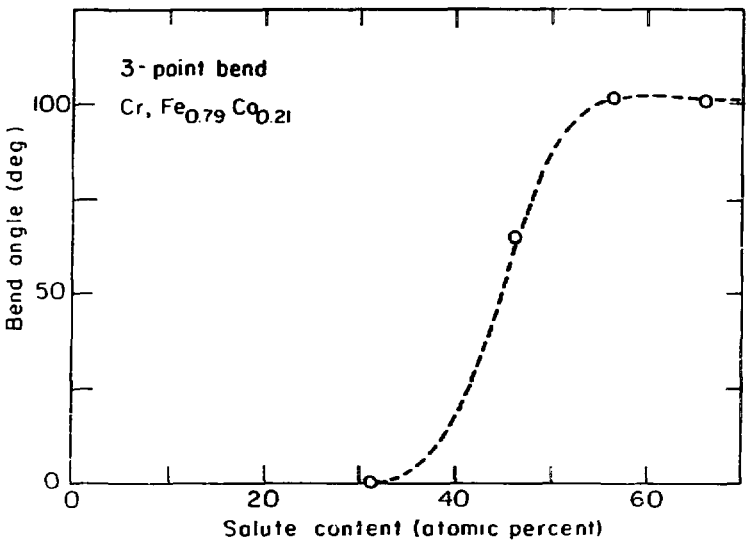

XBL 788-5574

Fig. 61